1 *This is a Preprint and has not been peer reviewed.*

Paleoseismology of the Zougahana fault, northern Aso

outer rim, and its role in the tectonics of northern

Kyushu

5 Keitaro Komura[1]*, Hiroshi P. Sato[2], Hiroshi Yagi[3], Takayuki Nakano[4], Hiroshi Une[5]

6

7 [1] Central Research Institute of Electric Power Industry, 1646 Abiko, Abiko-shi 270-

8 1194, Japan; email: komukeit@criepi.denken.or.jp

9 [2] Nihon University, College of Humanities and Science, 3-25-40, Sakura-Josui,

10 Setagaya-ku, Tokyo 156-8550, Japan

11 [3] Fukada Geological Institute, 2-13-12, Hon-Komagome, Bunkyo-ku, Tokyo 113-0021,

12 Japan

13 [4] Geospatial Information Authority of Japan, 1, Kitagou, Tsukuba 305-0811, Japan

14 [5] Ochanomizu University, 2-1-1, Otsuka, Bunkyo-ku, Tokyo 112-8610, Japan

15 * Corresponding author

16   **Key Points**

17   ・The Zougahana fault, ~14 km northeast of the primary fault, ruptured during the 2016

18   Kumamoto earthquake.

19   ・We identify ≥4 events on the Zougahana fault since 10 ka, triggered by strong

20   motions on the primary fault.

21   ・The Zougahana fault may not be a simple secondary fault, but part of the main

22   transtensional shear structure.

23   **Abstract**

24   The Kumamoto earthquake (M_j 6.5, M_j 7.3) occurred on 14 and 16 April 2016, with the

25   epicenter on the Futagawa and Hinagu faults, central Kyushu Island, southwest Japan.

26   Differential interferometric synthetic aperture radar analyses detected many phase

27   discontinuities in the source region. Phase discontinuities and ruptures were also

28   confirmed at the Zougahana fault on the northeastern rim of Aso caldera, approximately

29   14 km northeast of the Futagawa fault. In this study, we conducted topographic

30   interpretations, field surveys, outcrop descriptions/interpretations, and coring

31   investigations of the Zougahana fault. We clarified that at least four earthquake events

32   have occurred since 10 ka, including the 2016 earthquake. Among the events preceding

33   the 2016 earthquake, the ages of the most recent three were estimated to be 5780–2750

34   cal BP, 9020–7200 cal BP, and 9430–8450 cal BP based on tephra and radiocarbon ages

35   in the sediments. However, we note the possibility of missing events during 4350–1010

36   cal BP and 8690–5020 cal BP. Comparison with the paleoseismic history of the primary

37   Futagawa fault and surrounding secondary faults suggests that the Zougahana fault is

38   among the secondary faults that have repeatedly interacted with the Futagawa fault. The

39 distribution of aftershocks and our analysis of seismic intensity and Coulomb stress

40 change indicate that the trigger for the Zougahana fault may have been strong seismic

41 activity. However, secondary faults around Aso caldera, including the Zougahana fault,

42 may have slipped due to various triggers. Furthermore, within the transtensional

43 tectonics model, which views the complex of volcanoes, grabens, and strike-slip faults

44 that fan out across central Kyushu as a single unit, the Zougahana fault may not be a

45 simple secondary fault on the surface, but rather part of the main shear structure.

Introduction

The Futagawa and Hinagu faults are active faults in central Kyushu Island, Japan, and is

located on the southern edge of the Beppu-Shimabara graben zone (BSGZ)

(Matsumoto, 1979) (Fig. 1a, 1b). In 2016, successive earthquakes of M_j 6.5 (M_w 6.2) at

21:26 JST on 14 April and of M_j 7.3 (M_w 7.0) at 01:25 JST on 16 April occurred along

the Futagawa and Hinagu faults (the 2016 Kumamoto earthquake sequence; Earthquake

Research Committee, the Headquarters for Earthquake Research Promotion, 2016). In

this contribution, we use 'the 2016 Kumamoto earthquake' or 'the 2016 earthquake' to

refer to the main shock that occurred on 16 April. During this earthquake, a 30–34-km-

long right-lateral rupture occurred along the Futagawa and northern part of the Hinagu

faults from Mifune town in the southwest to Minami-Aso village in the northeast (Fig.

1c; Shirahama *et al.*, 2016; Kumahara *et al.*, 2022). Interferometric synthetic aperture

radar (InSAR) analysis of the 2016 earthquake confirmed numerous phase

discontinuities around the Futagawa and Hinagu faults (Fig. 1c; Fujiwara *et al.*, 2016).

Field surveys also revealed that some phase discontinuities had caused surface

deformations (Goto *et al.*, 2017; Ishimura *et al.*, 2021; Une *et al.*, 2022). In this study,

62   we refer to phase discontinuities confirmed in the field as secondary faults that are

63   distinct from the primary fault (here the Futagawa fault) following the definition by

64   Ishimura *et al*. (2021). Based on subsequent coring data and trench surveys, it is

65   becoming clear that some of these secondary faults have been activated repeatedly in

66   the past (Goto *et al*., 2017; Inoue *et al*., 2020; Ishimura *et al*., 2021; Sato *et al*., 2021).

67   Several interpretations have been offered for the triggering of secondary faults

68   associated with the 2016 Kumamoto earthquake in different regions. In the area of

69   Kumamoto city west of the Futagawa fault, the Suizenji fault zone (Fig. 1c) is thought

70   to have slipped due to the Coulomb stress change (ΔCFF, e.g., King *et al*., 1994)

71   associated with the rupture of the Futagawa fault (Goto *et al*., 2017). Many secondary

72   faults with a normal fault sense appeared in the Kuradake graben northwest of Aso

73   caldera (Fig. 1c) (Fujiwara *et al*., 2016; Une *et al*., 2022) and have been attributed to the

74   release of background north–south tensile stress triggered by the strong seismic motions

75   of the 2016 earthquake (Fujiwara *et al*., 2020). Furthermore, multiple NE–SW-trending

76   phase discontinuities were identified extending from the Futagawa fault's northeastern

77   end to the northeastern rim of Aso caldera. The Miyaji fault (Fig. 1c), which has the

78   same right-lateral sense as the Futagawa fault, is estimated to have repeatedly interacted

79   with the Futagawa fault in the past (Ishimura *et al*., 2021), although the triggering

80   mechanism is not yet understood. Toda and Ishimura (2019) showed that two secondary

81   faulting mechanisms occurred during the 2016 Kumamoto earthquake: ΔCFF triggering

82   and dynamic triggering, both due to the rupture of the Futagawa fault. The papers listed

83   above suggest that secondary faulting can be triggered by diverse mechanisms, even for

84   a single earthquake.

85   Clarifying the triggers of secondary faulting is important for assessing the

86   potential for off-fault displacements and impacts on important structures (e.g., IAEA,

87   2010; Petersen *et al*., 2011). In particular, secondary faults occurring along the direction

88   of extension of a strike-slip fault provide important data for evaluating the

89   characteristics of the fault tips, such as dispersion, extension, and step (Biasi and

90   Wesnousky, 2016, 2017; Kim and Sanderson, 2006; King and Nábělek, 1985; Lettis *et*

91   *al.*, 2002; Wesnousky, 1988, 2006). Together with this insight, central Kyushu Island

92   has a unique geological structure, featuring multiple active volcanoes and grabens

93   attributed to the oblique subduction of the Philippine Sea Plate (e.g., Hatanaka and

94   Shimazaki, 1988; Matsumoto, 1979; Chida, 1992; Ohashi et al., 2020). Understanding

95   whether secondary faulting that occurred in this tectonic setting is common or unique

96   compared to typical strike-slip fault systems will also contribute to a more accurate

97   evaluation of off-fault displacement hazards.

98   In this study, we focused on a phase discontinuity that appeared about 14 km

99   northeast of the Futagawa fault along its direction of extension, and which was

100   previously interpreted by Fujiwara *et al*. (2016) (Fig. 2). This phase discontinuity

101   appears to have been caused by activity on the Zougahana fault, a short fault

102   approximately 3.5 km long (Fig. 1c; Obata, 1998) that roughly matches the trend of the

103   phase discontinuity. The Zougahana fault occurs in a relatively fault-free area of the

104   BSGZ (Fig. 1b) and may be an important factor in understanding the tectonics of the

105   central Kyushu. Therefore, we conducted a paleoseismic field survey targeting the

106   Zougahana fault to clarify its activity and association with the Futagawa fault. We also

107   examined the trigger of the 2016 activity on the Zougahana fault from the perspectives

108   of seismology and geology. Based on our results, we considered the role of this fault in

109   the overall tectonics of central Kyushu.

Overview of the Zougahana D prehistoric site and geomorphology in the northeastern part of Aso caldera

110 111

112 The Futagawa fault, which was the source of the 2016 Kumamoto earthquake, is an

113 active fault with an NE–SW strike that extends from Kumamoto city center to Aso

114 caldera (Fig. 1c). In addition, several other relatively short active faults have been

115 identified around Aso caldera (e.g., Watanabe, 1984; The Research Group for Active

116 Tectonics in Kyushu, 1989; Suzuki *et al*., 2017). Of these, Watanabe (1984) identified a

117 group of NE–SW-trending active faults in the northern part of Aso caldera (black solid

118 lines in Fig. 1c). This group includes the Zougahana fault, which crosses the Zougahana

119 D prehistoric site (containing relics from the Paleolithic era) as a NE–SW strike fault,

120 with the northwest being the downthrown side (Obata, 1998). They stated that the

121 displacement caused by this fault cannot be explained by gravitational slumping toward

122 the northwest.

123 The Zougahana D prehistoric site is a plateau that juts southward into Aso caldera

124 at about 800 m elevation (Fig. 1c); the plateau is situated about 300 m above the caldera

125 floor. The lower part of the caldera wall (below 650 m elevation) is a moderate scarp,

126 whereas the upper part of the caldera wall (650–800 m elevation) forms a steep scarp.

9

127   According to Ono and Watanabe (1985), this steep scarp is composed of ejecta from

128   past large-scale eruptions at Aso caldera, including the lower Aso-1 pyroclastic flow

129   deposits (ca. 280–250 ka; Matsumoto *et al*., 1991), the Aso-2/1 lava (ca. 260–190 ka

130   and 150–140 ka; Matsumoto *et al*., 1991), the Aso-2 pyroclastic flow deposits (ca. 140

131   ka; Matsumoto *et al*., 1991), the Aso-3 pyroclastic flow deposits (ca. 130–120 ka;

132   Matsumoto *et al*., 1991), and the Aso-4 pyroclastic flow deposits (approx. 87 ka; Aoki,

133   2008) (Fig. 3a). Most of the pyroclastic flow deposits are welded tuffs. In particular, the

134   numerous black obsidian lithics found at the Zougahana D prehistoric site have been

135   confirmed to originate from the Aso-2 welded tuff of this caldera wall (Watanabe *et al*.,

136   2001). The upper part of the plateau is covered by thick volcanic ash and aeolian loam

137   that accumulated after the Aso-4 pyroclastic flow deposits.

138   The volcanic ash stratigraphy in the northeastern part of Aso caldera, including

139   the Zougahana D prehistoric site, was investigated in detail by Miyabuchi and

140   Sugiyama (2011). They integrated the results of tephra surveys at multiple locations

141   surrounding the Zougahana D prehistoric site and summarized the tephra stratigraphy

142   and vegetation changes over the past 90,000 years. Figure 3b is from their schematic

143   column, showing the shallowest 10 m below the ground surface. About twenty ash,

144   vitric ash, scoria, and pumice layers exist, but most are petrographically similar minor

145   tephras (e.g., YmS series; Miyabuchi, 2009) from the central cone in Aso caldera. They

146   are therefore difficult to distinguish as chronological indicators in the stratum.

147   Nonetheless, three tephras described below can be used as powerful age

148   indicators in the stratum. The most versatile is the Kikai Akahoya (K-Ah) tephra, which

149   erupted from the Kikai caldera in southern Kyushu at around 7.3 ka and is widely

150   distributed from the Kyushu region to western Japan; this tephra is identifying and

151   useful for dating Holocene soils (e.g., Machida and Arai, 2003). In the Aso region in

152   particular, it occurs as a distinct orange layer in the black soil just below the surface

153   (e.g., Miyabuchi and Sugiyama, 2011) and is easily identified by eye (Machida and

154   Arai, 2003). The Aira Tn (AT) tephra erupted from the Aira caldera in southern Kyushu

155   about 30 ka; it is also a highly versatile marker tephra that is used to date glacial

156   deposits throughout Japan (e.g., Machida and Arai, 2003). In the Aso region, it is often

157   recognized as being slightly lighter in color than the surrounding brown soil (e.g.,

158   Miyabuchi, 2009; Miyabuchi and Sugiyama, 2011). Although more difficult to identify

159   by eye than the K-Ah tephra, the AT tephra is easily identified based on the refractive

160   index of bubble-wall glass and major element analysis (Machida and Arai, 2003).

161   Another local tephra distributed around Aso is the Aso-Kusasenrigahama pumice (Kpfa;

162   Watanabe *et al*., 1982); distal deposits are also referred to as 'Aso-K' (Machida and

163   Arai, 2003). In the Aso area, it is recognized as a distinct orange pumice layer directly

164   below the AT tephra (e.g., Miyabuchi, 2009; Miyabuchi and Sugiyama, 2011). Recent

165   research on varves in Suigetsu Lake (central Japan) has constrained the eruption ages of

166   the K-Ah and AT tephras to 7303–7165 cal BP and 30,009 ± 189 cal BP, respectively

167   (Smith *et al*., 2013), and the eruption age of the Kpfa has been estimated as 32,647–

168   32,376 cal BP (McLean *et al*., 2020).

169   Obata (1998) classified the strata at the Zougahana D prehistoric site based on the

170   results of outcrop and pit excavations and clarified that the strata included the K-Ah,

171   AT, and Kpfa tephras, which could be identified by eye. They also described multiple

172   faults cutting through these tephra layers, displacing the Kpfa tephra by about 1.7 m.

173   Because all of these faults cut the loam layer containing the K-Ah tephra, they are

174   certainly active faults. However, Obata (1998) did not provide more detailed

12

175   information related to the displacement, such as the specific displacement amount of

176   each layer and the timing of fault activity. Maps and databases of active faults around

177   Aso caldera published since Obata (1998) do not include the trace of the Zougahana

178   fault (e.g., Nakata and Imaizumi, 2002; Suzuki *et al*., 2017; Imaizumi *et al*., 2018;

179   National Institute of Advanced Industrial Science and Technology, 2025), and detailed

180   paleoseismic investigations have not been conducted to this day.

181

182 **Method**

183 *Topographic and geological survey*

184 To understand the detailed topography around the Zougahana fault, we created a

185 morphometric protection index red relief image map (MPI-RRIM; Kaneda and Chiba,

186 2019) from a 1-m-resolution airborne light detection and ranging (LiDAR) digital

187 elevation model (DEM) acquired by the Kyushu Regional Development Bureau of the

188 Ministry of Land, Infrastructure, Transport and Tourism in 2010, i.e., before the 2016

189 Kumamoto earthquake. We conducted topographic interpretation using this MPI-RRIM.

190 Furthermore, to map the topography at the Zougahana D prehistoric site in more detail,

191 aerial photographs were acquired after the 2016 earthquake using a DJI Phantom 4 Pro

192 drone, from which a topographic map was generated. Before the drone photography, we

193 set eight Real Time Kinematic-Global Navigation Satellite System reference points

194 (Fig. 3a). Using those reference coordinates, we generated a three-dimensional image

195 using Structure from Motion and Multi-View Stereo (SfM-MVS) photogrammetry

196 software (Agisoft Metashape, professional version) and generated a contour map. We

197 also cut as much grass as possible over the 2016 rupture trace before the drone

198   photography. In addition, the wall of the surveyed outcrop and the location of the hand

199   coring survey described below were measured using a total station (Nikon DTM-503)

200   based on the aforementioned reference points. Furthermore, we conducted a surface

201   survey of the area around the Zougahana D prehistoric site to track the 2016 rupture,

202   search for fault outcrops, and confirm the surface geology.

203

204   *Measurement of the 2016 rupture*

205   Shirahama *et al*. (2016), Suzuki *et al*. (2017), and Kumahara *et al*. (2022)

206   comprehensively mapped surface ruptures of the 2016 Kumamoto earthquake, but did

207   not recognize surface ruptures along the Zougahana fault. However, our field survey

208   after the 2016 earthquake revealed a rupture in the paved road within the Zougahana D

209   prehistoric site. The rupture was not visible in the Google Earth image taken before the

210   earthquake, suggesting that this displacement formed during the 2016 earthquake. To

211   accurately evaluate this rupture's vertical and horizontal displacement, we measured a

212   paved road surface using a total station, referring to the reference points shown in

213   Figure 3a. The sideline's length was 50 m, and the distance between measurement

214   points was 0.5 m. However, in areas with rapid displacement, more narrowly spaced

215   points were used to measure displacement. The final measured displacement is reported

216   as a value with a plus or minus error, was determined by the method of Kaneda *et al*.

217   (2008) by creating best-fit lines with $\pm 1\sigma$ uncertainty drawn from the upthrown and

218   downthrown sides and then reading the minimum and maximum values within ± 20 m of

219   the fault and setting them as values with $\pm$ error.

220

221   *Detection of the up–down component of crustal deformation using InSAR*

222   To clarify the vertical movements around the Zougahana D prehistoric site due to the

223   2016 Kumamoto earthquake, a SAR interferogram was generated from PALSAR-2 data

224   (Table 1) acquired before and after the earthquake along ascending and descending

225   orbits, from which we estimated the quasi-vertical and horizontal movements around

226   the Zougahana fault. We used RINC ver. 0.43 (Ozawa *et al*., 2016) to process the

227   PALSAR-2 data and followed the 2.5-dimensional analysis method of Fujiwara *et al*.

228   (2000) to calculate the quasi-vertical and horizontal movements. In detail, each plane

229   includes two line-of-sight (LOS) deformation vectors perpendicular to (to the right of)

230   the ascending and descending orbits at all ground points in the SAR image. The quasi

231   up–down component was calculated as the two-dimensional deformation on the plane

232   approximately vertical to the ground point.

233

234   *Sketch of the Zougahana fault outcrop*

235   Obata (1998) described the Zougahana D prehistoric site (hereafter referred to as the

236   Zougahana fault outcrop), which is to the east of a paved road running north–south. The

237   Zougahana fault outcrop was covered by vegetation and alluvial soil at the time of our

238   survey. Although we planned to widen the outcrop using heavy machinery, it is in a

239   culturally protected area by local government, and we could not do so. Therefore, we

240   could only remove the surface vegetation and sediment from the existing outcrop and

241   observe and describe the outcrop in order to reconstruct the 2016 rupture and prior

242   displacements. While exposing the outcrop, we did not find any archaeological artifacts.

243   We exposed two walls: the north wall, about 4 m high and 7.5 m long north to

244   south, and the south wall, about 4 m high and 3.5 m long north to south. Although the

245   north and south walls are offset by about 1 m in the direction perpendicular to the wall's

246   surfaces (i.e., the north wall is further back when looking at the walls toward the east),

247   they are treated as continuous sections overlapping over a 1 m long section. Our final

248   sketch diagram connects the two walls accordingly. Using string, we constructed a grid

249   at 50 cm increments both walls and observed and described the detailed strata of the

250   wall surface and the location of the 2016 rupture. In addition, we took high-resolution

251   photographs of each grid cell to construct a 3D model and mosaic image of the wall

252   surface using SfM-MVS (Agisoft Metashape, professional version).

253

254   *Hand-coring survey*

255   To describe the stratigraphy of the formations below the Zougahana fault outcrop and to

256   identify key tephra layers, we used a hand auger to core down from the top of the fault

257   outcrop to a depth of 4 m at two locations; from those cores, we collected samples for

258   tephra analysis. We performed a similar hand auger survey at two sites along the paved

259   road to the northwest of the fault outcrop and at two sites along the paved road to the

260   southeast.

261

262 *Radiocarbon dating and tephra analysis*

263 To estimate the ages of the sedimentary layers, we collected charcoal materials and

264 organic soil samples from the outcrop wall for radiocarbon dating. For tephra analysis,

265 we collected blocks of soil measuring ca. 3 cm on each side from the hand auger cores

266 at locations where tephra was identified by eye.

267 Radiocarbon ages were obtained by accelerator mass spectrometry at the

268 Yamagata University High-Sensitivity Accelerator Mass Spectrometry Center after acid

269 and alkali treatment and sieving through a 250 μm sieve. We obtained uncalibrated

270 dates (yr BP).

271 The soil samples were sieved using a mesh cloth and an ultrasonic cleaner to

272 extract very fine ash particles (62.5–125 μm) for tephra analysis. The extracted particles

273 were observed under a polarizing microscope and volcanic glass shards were counted.

274 For samples in which a significant number of volcanic glass fragments were detected,

275 the refractive index was measured using a RIMS2000 refractometer (Kyoto Fission

276 Track Co., Ltd., Kyoto, Japan) at the department of civil and environmental

277 engineering, Chuo University, Tokyo, Japan. In addition, we analyzed the major

278   element compositions of some glass samples by wavelength dispersive spectroscopy

279   using a JEOL-JXA-8800 electron probe microanalyzer at the Central Research Institute

280   of Electric Power Industry, Chiba, Japan. We used the same analytical conditions as

281   Takeuchi *et al*. (2021), using the AT tephra as the standard.

282   Based on the ages obtained from radiocarbon dating and tephra analysis, we used

283   OxCal v.4.4 (Bronk Ramsey, 2024) and the IntCal20 calibration curve (Reimer *et al*.,

284   2020) to perform Bayesian estimation of the age of the event that displaced the strata. In

285   this study, we used the Sequence Model (Bronk Ramsey, 1995) to impose constraints on

286   the relative age of each age value when the lower strata were certainly older than the

287   upper strata, and the Phase Model (Bronk Ramsey, 2009) to treat age values for which

288   the relative ages were unclear (disturbed sediments or sampling locations) as a uniform

289   group. The calendar year calibration and model age values are reported as rounded

290   values (cal BP) with a confidence interval of $\pm 2\sigma$.

291

Results

Geomorphology, geology, and characteristics of the 2016 rupture around the

Zougahana D prehistoric site

Figures 4a and 4b show the MPI-RRIM and geomorphological map around the

Zougahana D prehistoric site. Around the Zougahana D prehistoric site, the plateau is

being eroded from east to west. Based on the geological map (Fig. 3a), most of the

plateau is covered by the Aso-4 pyroclastic flow (Fig. 4b). The erosion front can be

divided into two parts: an older erosion front and a fresher erosion front that erodes the

older. Part of the fresh erosion front coincides with the geological boundary between the

Aso-2/1 lava and the Aso-2A/2B pyroclastic flow (Fig. 3a), which may be a

geomorphological feature associated with different degrees of welding. To the northeast

of the Zougahana fault outcrop is a linear scarp with a N60°E–N70°E strike and a

height of 1.8–4.1 m (Figs. 4b, c, and 5a). Although it is not possible to rule out the

possibility that these linear scarp features were formed by fluvial erosion, the linear

valley morphology is unusual in this area, where a horseshoe-shaped erosion front

307   dominates (Fig. 4b); therefore, the linear valley morphology is likely due to repeated

308   fault displacement.

309   The mapped location of the 2016 rupture is shown in Figure 4b. A paved road

310   adjacent to the Zougahana fault outcrop was surveyed immediately after the earthquake,

311   and a rupture with a strike of N70°E and relatively northwest-downward displacement

312   was observed (Fig. 5b). Many 2016 ruptures were observed directly above the

313   Zougahana fault outcrop, and only two ruptures were found to the east of the outcrop

314   (Fig. 4b). Nonetheless, in the gorge on the southwest side of the Zougahana fault

315   outcrop (Loc. 1 shown in Figs. 3a, 4b), we discovered a new fault outcrop that had

316   not been described in previous studies (Figs. 5c, d). Although this location is situated on

317   Aso-2A/2B pyroclastic flow deposits (Fig. 3a), scarp deposits consisting mainly of

318   secondary/reworked deposits of the more recent Aso-4 eruptive phase are exposed on

319   the south side of the fault (Fig. 5d). On the valley floor, a small amount of welded tuff

320   was exposed on the south side of the fault, although the lithology of this deposit was

321   unclear. The fault at the boundary between the Aso-2A/2B pyroclastic flow deposit and

322   the scarp deposits strikes N65°E and dips 68°S (Fig. 5d), consistent with the strike of

22

323   the rupture observed on the paved road immediately adjacent to the Zougahana fault

324   outcrop. The fault identified at Loc. 1 is a normal south-dipping fault characterized by

325   an open rupture near the surface. The direction of vertical displacement is opposite that

326   of the northwest-dipping rupture identified on the paved road directly below the

327   Zougahana fault outcrop. Accordingly, the Zougahana fault is characterized by lateral

328   movement, with the apparent direction of vertical displacement changing locally.

329   Figures 6a and 6b show the results of the total station survey of the 2016 rupture,

330   which was conducted on the paved road directly below the Zougahana fault outcrop,

331   and show the horizontal and vertical displacements. The horizontal displacement shows

332   48.6 ± 0.2 cm of right-lateral slip, and the vertical displacement shows the north side of

333   the rupture dropping by 20.2 ± 4.7 cm. Therefore, the horizontal right-lateral slip is

334   more than twice the vertical displacement, consistent with our previous interpretation

335   that the dominant sense of slip is horizontal and that the apparent vertical displacement

336   direction changes locally.

337   Figure 7 shows the pseudo-vertical deformation derived from the InSAR analysis.

338   The northwest side of the fault subsided by up to 14 cm compared to the southeast side

339   adjacent to the Zougahana fault, consistent with the observed vertical displacement in

340   the field (Fig. 6b). Figure 7 includes two public triangulation points: Ogomori and

341   Kiotoshi. According to GNSS surveying by the Geospatial Information Authority of

342   Japan before and after the earthquake (Ootaki *et al.*, 2016), the relative displacement of

343   the Ogomori point relative to the Kiotoshi point was about 3 cm to the north and about

344   76 cm to the east, with 5 cm of subsidence. These survey results further support that the

345   right-lateral horizontal displacement was much greater than the vertical displacement.

346

347   *Description of the stratigraphy*

348   The mosaic photograph and interpretive sketch of the Zougahana fault outcrop are

349   shown in Figures 8a and 8b, respectively (see Supplement 1 for a 3D pdf file of the

350   outcrop). The north and south walls overlap at 6.5–7.5 m horizontally across the outcrop

351   (H6.5–H7.5), but the north wall is 1 m behind the south wall in the east–west direction

352   (into the page). Uncalibrated radiocarbon ages (yr BP) reported in Table 2 correspond to

353   the sample collection points in Figure 8b.

354   Obata (1998) conducted outcrop and small-scale pit excavation surveys around

355   the Zougahana fault outcrop and identified 25 units cut by 15 faults. Although it was not

356   possible to expose all the units defined by Obata (1998), we were able to observe units

357   corresponding to layers 1–9 as described by Obata (1998). We note that the

358   stratigraphic divisions, numbers, and fault names used herein are newly reclassified and

359   differ from those of Obata (1998). In identifying the units, we focused on the color,

360   consistency, powderiness, and continuity of the strata observed in the field. In our

361   classification, we recognized 12 units: the topsoil and units 10, 20, 30, 40, 50, 60, 70,

362   80, 90, 200, and 210. Units 10–60 were observed in the north face, and units 80–210 in

363   the south face, with unit 70 being common to both faces.

364   The surface soil includes the layer of grass and soil that covers both walls. The

365   soil is dark brown, and the radiocarbon age of sample 1 (south wall, H8.5, V1.5) is 381

366   ± 20 yr BP.

367   Unit 10 is a black soil layer 5–15 cm thick and rich in organic matter. The

368   radiocarbon age of sample 2 (north wall, H3.2, V1.5) is 1036 ± 20 yr BP.

369   Unit 20 is a dark brown soil layer 5–35 cm thick and less rich in organic matter

370   than unit 10. The radiocarbon age of sample 3 (north wall, H3.5, V1.5) is 2220 ± 20 yr

371   BP, and that of sample 4 (north wall, H5.7, V2.2) is 2668 ± 21 yr BP.

372   Unit 30 is a brown soil layer 35–80 cm thick and quite poor in organic matter. A

373   dark orange scoria, about 3–5 mm in diameter, is scattered throughout the unit 30 soil,

374   especially from H3.5 to H6.0.

375   Unit 40 is an inorganic light brown soil layer 15–25 cm thick. Orange patches 5–

376   10 mm in diameter are scattered throughout the soil layer west of H4.0. Based on the

377   type section for this area (Fig. 3b) and the description by Obata (1998), we correlate

378   these patches with the K-Ah tephra.

379   Unit 50 is a clayey dark gray soil layer 10–35 cm thick and poor in organic

380   matter. The boundary between units 50 and 40 is characterized by fissures and

381   undulations such as flame structures and involution, some of which are related to

382   deformation caused by the fault (described in the next subsection).

383   Unit 60 is a black soil layer 15–40 cm thick and rich in clay and organic matter.

384   We obtained six samples from unit 60 (samples 5–10) from the north face, and their

385   radiocarbon ages were 9297–8281 yr BP. According to Obata (1998), many artifacts

386   from the early Jomon period have been excavated from this layer.

387   Unit 70 is a grayish soil layer 15–55 cm thick; it is clay-like and poor in organic

388   matter. This unit is observed in both the north and south walls. According to Obata

389   (1998), this layer contains microlithic relics of Paleolithic age.

390   Unit 80 is a brownish soil layer 40–60 cm thick and poor in organic matter. The

391   bottom of unit 80 contains a band of scattered scoria with clasts ca. 2 mm in diameter.

392   This scoria is stratigraphically below the K-Ah tephra and above the AT tephra (Fig.

393   3b); it may correlate with one of the scoria-type volcanic ashes from Aso (e.g., YmS15

394   at 21 ka; Miyabuchi, 2009), but a more definite correlation is difficult. Similar to the

395   unit 50–40 boundary, undulations characterize the boundary between units 80 and 70,

396   some of which are related to deformation by the fault (described in the next subsection).

397   Unit 90 is a dark brown soil layer 10–50 cm thick (though we did not observe its

398   base) and moderately poor in organic matter. Sparse white scoria about 2 mm in

399   diameter are included at the top of this unit.

400   Unit 200 is an inorganic brown soil layer 55–65 cm thick. This unit is poorly

401   adhesive; soil particles fly out like a powder when the surface is cut with *Nisaku* twisted

402   sickle. Some scoria 2 mm in diameter are locally distributed at the top of this unit.

403   Unit 210 is an inorganic gray soil layer 45–100 cm thick (though we did not

404   observe its base) with a crunchy texture when cut with *Nisaku* twisted sickle. White

405   pumice is scattered in this unit. Fissures and undulations characterize the boundary

406   between units 210 and 200, similar to the unit 50–40 and 80–70 boundaries.

407   Based on their inorganic nature and lighter colors, units 200 and 210 imply

408   glacial deposits. Obata (1998) reported that the units below these contain the AT and

409   Kpfa tephras, though we could not confirm their presence by eye. Therefore, these

410   tephras are buried even deeper than the 210 exposed unit, and all units above unit 210

411   must be younger than the AT tephra (approx. 30 ka).

412

413   *Faults on the outcrop walls*

414   Numerous faults and open cracks were observed in the outcrop wall. Of these, the main

415   faults extending from the bottom of the wall surface and displacing the units were

416   numbered F1 to F7 from north to south (Fig. 8b). Although we observed the 2016

417   rupture directly above the surface soil in the range of H0.0–H4.5, no clear faults were

418   observed within the surface soil. It is possible that the displacement was dispersed by

419   unconsolidated soil and existing vegetation, making it difficult to trace the displacement

420   through the surface soil. We note that the fault names used herein are distinct from

421   those of Obata (1998), and we identified the faults independently.

422   Fault F1 was observed in the north wall, displacing the unit 30–20 boundary by

423   about 13 cm to the north. This displacement opened a crack up to 10 cm wide and 40

424   cm tall. Although we could not trace the fault upwards of unit 20, 2016 ruptures were

425   distributed on the ground surface above the top of F1. The unit 40–30 boundary was

426   also vertically displaced by about 4–15 cm, but it was not possible to determine whether

427   a clear vertical displacement occurred in the units below. We also observed an open

428   crack 3 cm wide and 10 cm tall near the unit 50–40 boundary (H2.1, V−0.1), and the

429   patchy K-Ah tephra contained in unit 40 had fallen out of place.

430   Fault F2 was observed in the north wall, and an open crack 5–10 cm wide and up

431   to 50 cm tall was observed near the unit 30–20 boundary. Slightly open cracks were

432   also observed in units 40–60. The clearest open crack was in unit 20, but could not be

433   traced into the units above, including unit 10. However, 2016 ruptures were distributed

434   on the ground surface, extending from the upper end of F2. F2 deformed the top of unit

435   20 by about 7 cm to the north and displaced the top of unit 30 by about 12 cm to the

436   north; it did not displace strata below unit 30.

437   In addition, a subordinate fault F2' split off of F2 towards the top of unit 40 and

438   developed into an open crack 10 cm wide and 10 cm tall near the top of unit 20. Like F1

439   and F2, the 2016 ruptures are distributed on the ground surface extending upward from

440   F2'. A small opening was observed in units 30–50, but became unclear near the bottom

441   of unit 60. We measured a northward displacement of about 3.6 cm at the top of unit 30.

442   Fault F3 was observed in the north wall, characterized by an open crack up to 10

443   cm wide and 10 cm tall cutting units 10 and 20 and another open crack up to 10 cm

444   wide and about 100 cm tall cutting units 30 and 40. Displacement was observed up to

445   the top of unit 10, and the 2016 rupture was observed in the direction of extension.

446   Although there was no clear vertical displacement at the unit boundaries, the top of unit

447   50 was displaced southward by 4.2–12.5 cm and the top of unit 60 was displaced

448   southward by 4.2–16.7 cm. In addition, we observed a fissure-fill structure, in which

449   units 50 and 60 open along F4 and the opening was filled by material from unit 40.

450   Fault F4 was observed in the north wall. We traced a slight crack in units 30–40

451   to at least the unit 30–20 boundary. Near the unit 60–50 boundary (H5.9, V1.2), F4 was

452   displaced 1–2 cm to the north (i.e., to the left of the wall surface) by fault F6 (discussed

453   below). We traced F4 to the base of the north wall, where it displaced the top of unit 60

454   by 9.2–36.7 cm to the north and the top of unit 70 by up to 9.2 cm to the south. We

455   attribute this apparent reversal of the sense of displacement to the lateral offset of the

456   units in three dimensions. Fissure-fill structures were observed in two locations in the

457   lower units, with unit 40 filling an opening in units 50 and 60 and unit 60 filling an

458   opening in unit 70.

459   Fault F5 was observed to be the longest fault in the exposed wall, extending from

460   the base of the south wall to the unit 30–20 boundary in the north wall. An open Y-

461   shaped crack was visible near the unit 40–30 boundary (H6.3, V1.4), and the fault

462   showed a complex, nested form. F5 was offset to the north (to the left side of the wall)

463   by approximately 3 cm where it crossed fault F6 (see next paragraph). Localized

464   openings also appeared near the top of unit 80 (H6.7, V0.6), below which the fault

465   showed complex branching in units 80 and 90. The fault displaced the top of unit 40 by

466   about 13 cm, unit 50 by about 18 cm, unit 60 by about 18 cm, and unit 70 by about 17

467   cm, all in a down-to-the-north sense. Although faults F1–F4 are high-angle faults, F5

468   showed characteristics of a reverse fault, dipping 50–60°S. In addition, we observed a

469   fissure-fill structure, with unit 40 dropping into units 50 and 60 and unit 60 dropping

470   into the opening in unit 70.

471   Fault F6 was observed as a north-dipping fault on the north wall, and the crack

472   extended upwards to the top of unit 20; although unclear, it seemed to continue into the

473   surface soil and near-surface. However, we did not observe any 2016 rupture on the

474   surface directly above F6. We also traced a clear fracture to the base of the north wall.

475   F6 appeared to have caused a northward displacement of about 9–16 cm at the top of

476   unit 40, displacing fault F5 by about 3 cm and fault F4 by 1–2 cm in the same direction.

477   Therefore, F6 must postdate faults F4 and F5, indicating relatively recent slumping.

478   Fault F7 was observed to be a south-dipping fault separating units 70–90 from

479   units 200–210 in the south wall. Because units 200 and 210 are interpreted to be glacial

480 deposits, their juxtaposition next to units 70–90 imply that F7 is a reverse fault that

481 pushed up sediments on the south side (the right side of the wall). F7 branched off

482 gradually at H8.7 and V0.5, and the leftmost branch terminated in unit 80. The top edge

483 of F7 showed an opening around 5–10 cm wide, and we confirmed that F7 reaches the

484 surface soil. Unit 80, which contains the scoria band in its lower portions, was displaced

485 vertically in multiple locations by F7, with northward displacement of about 3–17 cm at

486 the unit 80–70 boundary and about 10–12 cm at the unit 90–80 boundary. Unit 80 was

487 tilted about 20° northward toward the F7 fault from around H7.0, and we estimated the

488 total vertical displacement resulting from this tilting to be over 60 cm.

489

490 *Shallow subsurface structure of the fault*

491 Figure 9a shows the locations of the six hand coring sites, and Figure 9b shows

492 columnar sections for each core. The results of the tephra analysis conducted on each

493 hand core are summarized in Table 3. In addition, microphotographs of particles in each

494 tephra sample are shown in Figure S1 in Supplement materials. Major element

495 compositions of glass shards measured by electron probe microanalysis (EPMA) are

496 reported in Table S1 in Supplement materials.

497   Core ZH-1 consists of surface soil and black soil (about 0.40 m thick), dark

498 brown soil (about 0.35 m thick), and light brown soil (at least 3.2 m thick) from top to

499 bottom. However, as the core was excavated immediately next to a paved road, it is

500 possible that the top layer was cut off during the excavation of the road. We observed a

501 scoria layer approximately 3 cm thick at around 0.45 m depth, a volcanic ash layer

502 approximately 4 cm thick and a scoria layer approximately 2 cm thick at around 1.25–

503 1.40 m depth, a volcanic ash layer approximately 2 cm thick and a scoria layer

504 approximately 2 cm thick at around 2.5 m depth, and a sandy volcanic ash layer

505 approximately 10 cm thick at around 2.75 m depth. Although expected to appear in the

506 core, we did not observe the K-Ah tephra; therefore, it is likely that the surface layer

507 containing at least the K-Ah tephra was removed during excavation.

508   Core ZH-2 was cored about 10 m south of the ZH-1 core; it is likely that the

509 surface layer was also removed during excavation at this site. From top to bottom, we

510 identified the following layers: surface soil (about 0.10 m thick), dark brown soil (about

511 0.35 m thick), light brown soil (about 1.05 m thick), dark brown soil (about 0.95 m

512 thick), and alternating layers of light brown soil and black soil (at least 1.5 m thick).

513 Among these, we identified three scoria layers approximately 3–4 cm thick at 0.48–0.75

514 m depth, a scoria layer approximately 5 cm thick at 1.30 m depth, a scoria layer

515 approximately 2 cm thick at 2.2 m depth, a sandy volcanic ash layer approximately 2

516 cm thick at 2.49 m depth, a sandy volcanic ash layer approximately 22 cm thick at 3.10

517 m depth, an orange-colored tephra layer about 14 cm thick at about 3.47 m depth, and

518 an orange-colored tephra layer least 20 cm thick at about 3.90 m depth. We expected the

519 sandy tephra layer at 3.10 m depth ('2-122') to be the major tephra due to its thickness

520 of about 22 cm. The refractive index (Table 3) and major element composition of the

521 volcanic glass (Fig. 10) are consistent with the characteristics of the AT tephra;

522 accordingly we interpret this layer to be a pure AT tephra layer. Therefore, based on the

523 tephra stratigraphy of the surrounding area (Fig. 3b) and the description of the AT

524 tephra in a previous study of the Zougahana outcrop (Obata, 1998), either the orange-

525 colored volcanic ash layer at 3.47 m depth ('2-136') or the orange-colored volcanic ash

526 layer at 3.90 m depth ('2-150') may correspond to the Kpfa tephra. However, the major

35

527   element compositions of sample 2-153 do not match the compositional range of the

528   Kpfa tephra correlated with lake Suigetsu by McLean *et al.* (2020) and is less

529   differentiated (lower SiO_2 content; Fig. 10). Ishimura *et al.* (2022) conducted a trench

530   survey at the Futagawa fault west of the Aso caldera (Fig. 1c); they also recognized

531   volcanic glass with a composition similar to that of the upper part of the Kpfa tephra,

532   and our sample 2-153 may be correlated with the same glass as that of Ishimura *et al.*

533   (2022). According to the model tephra stratigraphy northeast of Aso (Fig. 3b;

534   Miyabuchi and Sugiyama, 2011), a relatively thick sandy ash is recognized directly

535   above Kpfa, although it is not named. Samples 2-153 in this study and the upper Kpfa

536   deposits in Ishimura *et al.* (2022) may be correlated to this sandy tephra. Regardless,

537   because this sandy ash occurs somewhere between the AT and Kpfa tephras, it must

538   have erupted between 32 and 30 ka.

539   Core ZH-3 was obtained from the top of the Zougahana fault outcrop wall and

540   overlaps the stratigraphy identified in the wall sketch below around V1.5. From top to

541   bottom, we recognized the following strata: surface soil (about 0.63 m thick), dark

542   brown soil (about 1.60 m thick), black soil (about 0.47 m thick), dark brown soil (about

543   0.55 m thick), and light brown soil (at least 0.75 m thick). Among these, we observed a

544   volcanic ash layer about 1 cm thick at about 0.86 m depth, a sandy volcanic ash layer

545   about 25 cm thick at about 1.73 m depth, a sandy volcanic ash layer about 5 cm thick at

546   about 2.27 m depth, and a scoria layer about 2 cm thick at about 3.96 m depth. The

547   sandy tephra layer at 1.73 m depth corresponds to the K-Ah tephra in unit 40 when

548   compared to the wall sketch (Fig. 8b). Similarly, the scoria layer at approximately 3.96

549   m depth in the core ('3-106') may correspond to the scoria in unit 80 of the south wall.

550   Core ZH-4 core was obtained from the surface of the Zougahana fault outcrop

551   wall and overlaps the stratigraphy identified in the wall sketch below around V2.5 (Fig.

552   8b). From top to bottom, we identified the following layers: surface soil and black soil

553   (about 0.60 m thick), dark brown soil (about 1.10 m thick), black soil (about 0.50 m

554   thick), dark brown soil (about 0.45 m thick), and light brown soil (at least 0.90 m thick).

555   Among these, we identified a volcanic ash layer about 1 cm thick at about 0.46 m depth,

556   a sandy volcanic ash layer about 17 cm thick at about 1.35 m depth, and a scoria layer

557   about 6 cm thick at about 3.23 m depth. The sandy volcanic ash layer 17 cm thick at

558   1.35 m depth in the core ('4-38') is correlated with the K-Ah tephra based on the wall

559   sketch (Fig. 8b). Similarly, the scoria layer at 3.23 m depth in the core ('4-94') may

560   correspond to the scoria in unit 80 of the south wall.

561   Core ZH-5 was obtained from the base of the wall at around H8.0 in the wall

562   sketch of the Zougahana fault outcrop, and samples below unit 90 in the wall sketch.

563   From the surface to 3.0 m depth, the soil was all light brown. Therein, we observed a

564   volcanic ash layer approximately 1 cm thick at around 0.54 m depth, a sandy volcanic

565   ash layer approximately 2 cm thick at around 0.75 m depth, an orange sandy volcanic

566   ash layer approximately 2 cm thick at around 1.82 m depth, a patchy orange volcanic

567   ash layer approximately 6 cm thick at around 1.97 m depth, a volcanic ash layer about 8

568   cm thick at about 2.46 m depth, and an orange volcanic ash layer about 4 cm thick at

569   about 2.82 m depth. The refractive index of the volcanic glass in the sandy volcanic ash

570   layer at 1.82 m depth ('5-65') is consistent with the AT tephra value (Table 3), and we

571   correlate it to the AT tephra accordingly. Therefore, based on core ZH-2, the orange-

572   colored volcanic ash at 2.80 m depth ('5-99'), which is approximately 1 m below the

573   AT tephra, may be comparable to the sandy ash above the Kpfa tephra.

574   Core ZH-6 was excavated next to a paved road on the south side of the fault. It

575   shows the following sequence from top to bottom: surface soil (about 0.30 m thick),

576   dark brown soil (about 0.30 m thick), light brown soil (about 2.63 m thick), and dark

577   brown soil (at least 0.76 m thick). However, as in the ZH-1 and ZH-2 cores, some of the

578   surface soil may have been removed during road construction. We observed a volcanic

579   ash layer approximately 5 cm thick at around 0.47 m depth, a volcanic ash layer

580   approximately 2 cm thick at around 0.59 m depth, a sandy volcanic ash layer

581   approximately 2 cm thick at around 1.69 m depth, a volcanic ash layer approximately 2

582   cm thick at around 3.28 m depth, and a volcanic ash layer at least 5 cm thick starting at

583   3.89 m depth. Nonetheless, we did not identify any major tephras in core ZH-6 that

584   could be used as age indicators, and the overall age of the core remains unknown.

585   However, given that the F7 reverse fault exists between cores ZH-5 and ZH-6, the

586   sediments identified in ZH-6 may be even older than the AT and Kpfa tephras.

587   Figure 11 presents the elevations and positions of the hand auger cores relative to

588   the Zougahana fault outcrop sketches as a cross section based on the total station survey

589   projected along the paved road (line A–B; Fig. 9a). In the outcrop (Fig. 8b), unit 40 and

590   the K-Ah tephra were displaced 4–16 cm vertically by each of the F1, F5, and F6 faults

591   (Fig. 8b) for a total displacement of 26–31 cm. Because the fault may have caused more

592   extensive vertical deformation, these values represent the minimum displacement of the

593   K-Ah tephra. However, the displacements of the volcanic ash and scoria layers below

594   the K-Ah tephra were greater, emphasizing the cumulative displacement of fault. The

595   relative heights of the scoria layers in unit 80 in the south wall and in core ZH-4 (and

596   perhaps ZH-3) indicate a maximum vertical offset of 2.9 m across faults F1–F6 (Fig.

597   11). Additionally, the relative heights of the AT tephra in cores ZH-2 and ZH-5 indicate

598   a vertical offset of approximately 2.6 m across faults F1–F6 (Fig. 11). Although the

599   positions of the unit 80 scoria and AT tephra are unknown on the south side of fault F7,

600   that fault is a reverse fault and the vertical displacements of both tephras are expected to

601   be even greater than the above values when accounting for fault F7. The reason for the

602   30 cm displacement discrepancy between the unit 80 scoria and AT tephra remains

603   unknown. However, given that the locations of the cores were projected along the

604   pavement and the units are offset in 3D due to lateral movement, we consider this value

605   to be within the margin of error. Regardless, our results clearly highlight a cumulative

606   displacement between the deposition of the AT tephra (ca. 30 ka) and the K-Ah tephra

607   (ca. 7.3 ka).

608

609   *Paleoearthquakes and age constraints for the Zougahana fault outcrop*

610   In our detailed observation of the Zougahana fault outcrop, we inferred multiple

611   displacement events based on faultings and deformation structures like fissure-fill,

612   flame, undulation, and abut observed at the top surface of each unit. In addition, the

613   deformation structures of faults F5, F7, and the surrounding areas (Fig. 8b), which had

614   the best continuity and were the most straightforward to interpret, were useful for

615   recognizing events. In this subsection, we identify events, including the 2016

616   earthquake, from the most recent to the oldest.

617   The 2016 rupture at the ground surface was distributed over a width of about 4.5

618   m (H0.0–H4.5), but there was no clear fault corresponding to the 2016 rupture in the

619   outcrop (Fig. 8b). Accordingly, we interpret that the displacements observable in the

620   outcrop are part of the positive flower structure (e.g., Fossen 2016) associated with right

621   lateral offset, and that this distributed displacement is expressed as flexural

622   displacement at the ground surface. The wall surface also showed many fresh open

623   cracks and fissures that had not yet been filled with sediment, which we attribute to the

624   2016 earthquake, consistent with a trench survey of the Futagawa fault conducted after

625   the 2016 earthquake (Ishimura *et al*., 2022). Since all faults in the outcrop were

626   accompanied by fresh open cracks and fissures, it is likely that all faults moved during

627   the 2016 earthquake. In particular, faults F1–F3 on the north side have large apertures

628   and are consistent with the locations of the 2016 ruptures at the ground surface,

629   suggesting that most of the displacement during the 2016 earthquake occurred along

630   these faults. Figure 12a is a sketch of the Zougahana fault outcrop (Fig. 8b) focused on

631   the area around faults F5 and F7 in the range H5.0–H9.0, V0.0–V3.0. By removing all

632   open cracks and fissures thought to have formed due to the 2016 earthquake, we

633   estimate the pre-2016 earthquake wall surface appeared as in Figure 12b. Fault F6,

634   which reached the surface and shifted fault F5 by about 3 cm and fault F4 by 1–2 cm to

635   the north (left side of the outcrop), is thought to be a slump fault that formed as a result

636   of the 2016 earthquake, and we have retro-deformed this displacement in Figure 12b.

637   We estimate that the penultimate event occurred before the deposition of unit 20

638   because faults F4 and F5 are interrupted at the unit 30–20 boundary, and the

639   displacement at the unit 40–30 boundary caused by fault F5 cannot be attributed to the

640   2016 displacement. Hereafter, we refer to this event as 'Event 1'. Figure 12c shows the

641   estimated wall surface immediately after Event 1. By retro-deforming the displacement

642   of fault F5 to zero displacement at the unit 40–30 boundary, we obtain the estimated

643   pre-Event 1 wall surface shown in Figure 12d.

644   We estimate that the antepenultimate event ('Event 2') occurred before the

645   deposition of unit 40. Although the unit 50–40 boundary is deformed like a flame

646   structure, the top surface of unit 40 is inconsistently relatively flat, suggesting that

647   deformation occurred when the unit 50–40 boundary was at the surface. Furthermore,

648   material from unit 40 fills fissures along faults F4 and F5 in units 50 and 60.

649   Accordingly, Figure 12e shows the estimated wall surface immediately after Event 2.

650   By restoring the deformation at the surface of unit 50 as well as along the fissures, we

651   estimate that the pre-Event 2 wall surface was as shown in Figure 12f. Importantly, this

652   reconstruction requires that the K-Ah tephra was deposited after Event 2 (Fig. 12d).

653   According to Figure 12f, unit 50 (dark gray soil layer) is thicker to the north (left)

654   and appears to abut unit 60. Therefore, when the deposition of unit 50 began, it is

655   possible that the ground surface to the south (right) was already uplifting, and we

656   estimate that the preceding event ('Event 3') occurred before the deposition of unit 50.

657   We consider that the flame structure and fissures at the unit 60–50 boundary is due to

658   Event 3, but it could have also formed underground during Event 2. Figure 12g shows

659   the estimated wall surface immediately after Event 3. By correcting the deformation of

660   unit 60 and rotate the section to have a flat surface, we obtain the pre-Event 3 wall

661   surface shown in Figure 12h.

662   We estimated the event preceding Event 3 ('Event 4') based on the clear fissure-

663   fill structure and undulation caused by fault F5 at the unit 80–70 boundary. We interpret

664   that Event 4 occurred after the deposition of unit 80 and caused the ground surface to

665   open; the subsequent deposition of unit 70 filled the fissure. Figure 12i shows the

666   estimated wall surface immediately after Event 4, from which we obtained the pre-

667   Event 4 wall surface by restoring deformation (Fig. 12j).

44

668   The F7 fault in the south wall displaced the upper surface of unit 90, and at least

669   one of the branches of this fault appears to terminate within unit 80. Therefore, it is

670   possible that an event occurred during the deposition of unit 80 ('Event 5'). Figure 12k

671   shows the estimated wall surface immediately after Event 5, from which we obtained

672   the pre-Event 5 wall surface by restoring deformation and tilting until we achieved a flat

673   surface for unit 80 (Fig. 12l) is estimated. Furthermore, because white scoria is scattered

674   below unit 80, Event 5 must have occurred after deposition of this scoria.

675   To the south of fault F7, older deposits (units 200–210) extend further south (Fig.

676   8b). Furthermore, we estimated 2.6 m of cumulative vertical displacement of the AT

677   tephra from our hand core results (Fig. 11), but this displacement cannot be explained

678   by the cumulative vertical displacements of Events 1–5 estimated so far. Therefore,

679   numerous events must have preceded Event 5.

680   Figure 13 shows the vertical displacements measured on faults F1–F7 at each

681   stratum boundary in the wall of the Zougahana fault outcrop (Fig. 8b), as well as the

682   unit levels of Events 1–5 and the 2016 earthquake. This figure highlights discrepancies

683   between the displacements along fault F2 at the unit 20–10 and unit 30–20 boundaries,

684   and along fault F5 at the unit 40–30 and unit 50–40 boundaries, for which we have not

685   identified any event. Therefore, it is possible that 'missing' events for which we have no

686   direct evidence in this outcrop occurred in these two sections (i.e., during the deposition

687   of unit 20 and unit 40; 'PM Event 0.5' and 'PM Event 1.5', respectively). As we will

688   discuss in more detail later subsection *Comparison with paleoseismic events on*

689   *the Futagawa fault and other secondary faults*, other events identified on the

690   Futagawa fault and its surrounding secondary faults occurred during the period of

691   deposition of unit 20 (e.g., Ishimura *et al*., 2021, 2022; Sato *et al*., 2021), supporting our

692   interpretation of missing events on the Zougahana fault. However, such small

693   differences in fault displacement in the trench wall can also be explained by the upper

694   attenuation of fault displacement (Ishimura *et al*., 2017).

695   In summary, we identified six past events (the 2016 event and Events 1–5) in the

696   Zougahana fault outcrop. We constructed a chronological model using OxCal based on

697   the uncalibrated radiocarbon ages (yr BP) obtained from the wall and the results of

698   tephra analysis to calibrate and constrain these event dates (Fig. 14a). In this model, we

699   ignore the possible missing events ('model A'). The code for the constructed OxCal

700   model is shown in Text S1 in Supplement materials. In this case, we adopted ages of the

701   K-Ah tephra identified in the wall and of the AT tephra (taken as the lower limit of the

702   earliest event) to be 7303–7165 cal BP and 30,009 ± 189 cal BP (Smith *et al.*, 2013),

703   respectively. According to the model chronology, Event 1 (thought to have occurred at

704   the unit 30–20 boundary) is estimated to have occurred at 5780–2750 cal BP, Event 2

705   (unit 50–40 boundary) at 9020–7200 cal BP, and Event 3 (unit 60–50 boundary) at

706   9430–8450 cal BP. Events 4 (unit 80–70 boundary), 5 (during deposition of unit 80),

707   and the multiple earlier events for which constraining radiocarbon ages and tephra are

708   not available are collectively estimated to have occurred between 29,850 and 10,960 cal

709   BP (Fig. 14a) assuming the AT tephra as the oldest age constraint.

710   We also expanded the OxCal model to include the possible missing events during

711   the deposition of units 20 and 40 ('model B', incorporating PM Events 0.5 and 1.5; Fig.

712   13). Although this is a hypothetical age estimation, if these two possible events did

713   occur, the OxCal Model returned an age range of 4350–1010 cal BP for PM Event 0.5, a

714   modified age range of 5790–2750 cal BP for Event 1, and a range of 8690–5020 cal BP

715   for PM Event 1.5 (Fig. 14b). The OxCal code of model B is also shown in Text S2 in

716   Supplement materials.

717

718 Discussion

719 *Comparison with paleoseismic events on the Futagawa fault and other*

720 *secondary faults*

721 We estimated that at least six earthquake events, including the 2016 earthquake, can be

722 concluded to have occurred on the Zougahana fault. In particular, four events are

723 estimated to have occurred since 10 ka (model A; Fig. 14a). In addition, we expanded

724 the model to incorporate possible missing events (PM Event 0.5, PM Event 1.5), in

725 which case we estimated the at least eight earthquakes have occurred (model B; Fig.

726 14b). The average recurrence interval of events from just before the occurrence of Event

727 3 to just after the 2016 earthquake, which were estimated with relatively high accuracy,

728 was calculated to be approximately 2800–3200 years for model A and approximately

729 1700–1900 years for model B. Assuming these average recurrence intervals to have

730 remained constant, these values correspond to the occurrence of 9–10 events (model A)

731 or 15–17 events (model B) since the deposition of the AT tephra ca. 30 ka. The vertical

732 displacement of the 2016 earthquake measured on the paved road in front of the

733 Zougahana fault outcrop was 20.2 ± 4.7 cm (Fig. 6b); if this is characteristic slip during

49

734   a single event, the cumulative displacement since the AT tephra fall is 1.93 ± 0.56 m

735   (model A) or 3.28 ± 0.95 m (model B). Given that the vertical displacement of the AT

736   tephra based on our group-sequence coring was estimated to be about 2.6 m (Fig. 11),

737   model B, which has an overlapping error range, appears more consistent. However,

738   because the vertical displacement of the lateral fault may have differed in each event

739   (e.g., Petersen *et al*., 2011), these calculations are for reference only.

740   Multiple trench surveys have been carried out on the Futagawa fault since the

741   2016 Kumamoto earthquake (Ueta *et al*., 2018; Okamura *et al*., 2018; Toda *et al*., 2019;

742   Kumahara *et al*., 2017; Iwasa *et al*., 2022; Ishimura *et al*., 2022; Tsutsumi *et al*., 2018).

743   Among these, Ishimura *et al*. (2022) reconstructed a reliable paleoseismic history of the

744   Futagawa fault based on multiple pit excavation surveys. They concluded that four fault

745   events (including the 2016 event) occurred after the K-Ah tephra fall, and estimated the

746   ages of the three events preceding the 2016 event to be 2150–1460 cal BP, 4310–2940

747   cal BP, and 6030–4360 cal BP (Fig. 15a). In particular, the penultimate event (2150–

748   1460 cal BP) has been confirmed in several other trench surveys along the Futagawa

749   fault (Iwasa *et al*., 2022; Toda *et al*., 2019). In model A of this study, we did not

750   identify any events corresponding to the penultimate event on the Futagawa fault, and

751   we only found evidence for one other event since the deposition of the K-Ah tephra

752   (Fig. 15b). Accordingly, we consider that our model B, including possible missing

753   events (Fig. 15c), may be the better model. Of course, it is not certain that activity on

754   the Zougahana fault has always accompanied activity of the Futagawa fault, and it may

755   have reacted only once or several times. Nonetheless, similarly timed events were

756   identified on the Miyaji fault (a secondary fault about 5 km south of the Zougahana

757   fault; Fig. 1c) at 2080–1830 cal BP (Ishimura *et al*., 2021; Fig. 15d) and on the

758   Matoishi-Bokujo I (MB I) fault (a secondary fault about 10 km away and belonging to

759   the Kuradake graben on the northwest side of the outer rim of Aso caldera; Fig. 1c)

760   sometime since 2810 cal BP (Sato *et al*., 2021; Fig. 15e). The paleoseismic histories of

761   these secondary faults are consistent with our model B of the Zougahana fault, implying

762   the existence of PM Event 0.5. Additional trench surveys to better determine the

763   paleoseismic history of the Zougahana fault should yield further data for comparison.

764

765   *What is the driving force of the Zougahana fault?*

766   The paleoseismic record shows that the Zougahana fault has repeatedly interacted

767   with the Futagawa fault in the past. But what drove the movement on the Zougahana

768   fault during the 2016 Kumamoto earthquake? This pressing question needs to be

769   answered to better evaluate the behavior of active strike-slip faults. In this section, we

770   will consider this question from the perspectives of the aftershock distribution, strong

771   ground motions, and ΔCFF associated with the main shock.

772

773   *Background seismicity and aftershock distribution*

774   Figure 16 shows shallow background seismicity (<20 km depth) from the northeastern

775   part of the source region of the 2016 Kumamoto earthquake to Mt. Yufu, Oita

776   Prefecture, as well as the distribution of aftershocks since the main shock on 16 April

777   2016. This figure includes the locations of the Zougahana, MB I, and Miyaji faults,

778   which are considered to have triggered slip during the 2016 Kumamoto earthquake and

779   may have repeatedly interacted in the past.

780   According to the background seismicity during the 10 years preceding the 2016

781   Kumamoto earthquake, earthquakes occurred only sparsely along the Futagawa fault

782   and in the northern part of the caldera (Fig. 16a). In addition, shallow earthquakes of

783   volcanic origin occurred around the active volcanoes Mt. Yufu and Mt. Kuju. However,

784   there is no linear distribution of seismic sources along the strike of the Zougahana fault.

785   After the mainshock occurred at 01:25 JST on 16 April, active aftershocks were

786   observed at ~10 km depth in the northern part of Aso caldera, including the Zougahana

787   fault, without any time lag (Fig. 16b). In contrast, there exists a gap in aftershocks from

788   the northeastern end of the Futagawa fault to the area around the Zougahana fault,

789   known as the "Aso gap" (Uchide *et al*., 2016; Yoshida *et al*., 2017). The Aso gap has

790   traditionally been attributed to the existence of a low-density body underground

791   (Miyakawa *et al*., 2016); recent InSAR analyses and precise gravity observations have

792   revealed that a hydrothermal system has created a low-stress state that prevented the

793   propagation of the rupture (Kobayashi *et al*., 2025). In addition, a M_j 5.7 earthquake

794   occurred near Mt. Yufu, approximately 55 km northeast of the Futagawa fault, at the

795   same time as the main shock. It is clear in Figure 16b that aftershock activity near Mt.

796   Yufu had begun at that time. Indeed, numerous studies have shown that the seismic

797   motion accompanying the main shock of the 2016 Kumamoto earthquake triggered this

798 earthquake near Mt. Yufu (Uchide *et al*., 2016; Miyazawa, 2016; Yoshida, 2016; Saito

799 et al., 2025).

800   Next, 1 to 2 hours after the main shock, aftershocks continued around the

801 Zougahana fault at ~10 km depth, with the largest (M_j 5.9) occurring at 03:03 JST (Fig.

802 16c). Furthermore, within 2–3 hours after the main shock, aftershock activity around the

803 Zougahana fault extended further to the northeast, and at 03:55 JST, a M_j 5.8 aftershock

804 occurred southwest of Mt. Kuju (Fig. 16d). Three to six hours after the main shock,

805 aftershocks continued along the Zougahana fault and near Mt. Kuju, and at 07:11 JST, a

806 relatively large M_j 5.4 aftershock again occurred near Mt Yufu (Fig. 16e). Figure 16f

807 shows the distribution of aftershocks that occurred over the following month.

808 Aftershocks along the Zougahana fault and near Mt. Kuju and Mt. Yufu continued. On

809 18 April, a M_j 5.8 aftershock occurred southwest of Mt. Kuju, and on 29 April, a M_j 4.5

810 aftershock occurred southeast of Mt. Yufu (Fig. 16f).

811   Based on the aftershock distribution, aftershock activity occurred immediately

812 after the main shock at ~10 km depth directly below the Zougahana fault, and

813 aftershocks propagated northeasterly from there to southwest of Mt. Kuju during the 2–

814   3 hours following the main shock. Mt. Kuju appears to be an obstacle (the 'Mt. Kuju

815   wall') to aftershocks heading farther northeast. In addition, aftershock activity increased

816   near Mt. Yufu, even farther from the epicenter. Given the gap in aftershock activity

817   between Mt. Kuju and Mt. Yufu, the aftershocks from the Zougahana fault did not

818   propagate there.

819   Focusing on the MB I and Miyaji faults, some shallow seismicity occurred around

820   the MB I fault before the main shock, but no aftershocks occurred there, and almost no

821   background earthquakes or aftershocks occurred around the Miyaji fault. Therefore, two

822   secondary fault patterns occurred during the 2016 Kumamoto earthquake: one with

823   aftershocks, including the Zougahana fault, and one without.

824

825   *Seismic intensity*

826   Figure 17a shows the estimated seismic intensity distribution associated with the main

827   shock of the 2016 Kumamoto earthquake. The center of the Futagawa fault experienced

828   strong vibrations exceeding 6+ on the Japan Meteorological Agency (JMA) seismic

829   intensity scale, and it is estimated that the Zougahana and MB I faults were also hit by

830   stronger tremors compared to the surrounding areas that experienced JMA seismic

831   intensity 6−. In particular, the Zougahana fault is a hill-like landform isolated from its

832   surroundings, and seismic motions could be further amplified by the topographic effect

833   on earthquake motions (e.g., Boore, 1972). In contrast, the Miyaji fault, which was also

834   triggered by the main shock, did not experience strong shaking compared to

835   surrounding areas, registering JMA seismic intensities of 5− to 5+. In comparison, some

836   areas in the Mt. Yufu region experienced strong seismic shaking at JMA seismic

837   intensities of 6− to 6+, considered to result from the M_j 5.7 earthquake that occurred

838   almost simultaneously with the main shock (Uchide *et al*., 2016; Miyazawa, 2016;

839   Yoshida, 2016).

840

841   *Δ CFF*

842   We investigated ΔCFF to the northeast of the Futagawa fault. Many models have been

843   proposed for the Futagawa fault rupture associated with the main shock, as well as

844   various theories about the northeast end of the rupture (e.g., Asano and Iwata, 2016;

845   Himematsu and Furuya, 2016; Ozawa *et al*., 2016; Yoshida *et al*., 2017; Yue *et al*.,

846   2017; H. Kobayashi *et al*., 2017; Zhang *et al*., 2018; T. Kobayashi *et al*., 2025). Some

847   models include the Zougahana fault and the surrounding area as the source fault,

848   crossing Aso caldera (Kubo *et al*., 2016; Uchide *et al*., 2016). Here, however, we

849   adopted the fault model estimated based on crustal deformation data from the

850   Geospatial Information Authority of Japan (Yarai *et al*., 2016) and analyzed ΔCFF. The

851   reason for this is that in the northeastern end of the model of Yarai *et al*. (2016), the

852   western end of Aso caldera coincides well with the northeastern end of the surface

853   rupture (Shirahama *et al*., 2016; Kumahara *et al*., 2022) (Fig. 1c). This location is also

854   where the surface rupture dispersed, like the tip of a broom (e.g., Kim and Sanderson,

855   2006). We used Coulomb 3.3 software (Toda *et al*., 2011) to calculate ΔCFF, with

856   Poisson's ratio set to 0.25 and Young's modulus to 80 GPa.

857   Here, we assume that the Zougahana fault is a pure right-lateral strike-slip fault.

858   The results of the calculations showed that the Zougahana fault belongs to the -0.1 to -

859   0.7 bar value range and shows slight negative ΔCFF values (Fig. 17b). In addition,

860   Figures 17c and 17d show the results of our analysis when the Zougahana fault was

861   assumed as the south- and north-dipping oblique slip fault, considering the vertical

862   displacement from the 2016 earthquake (Fig. 5b). The shape of ΔCFF is almost the

863   same in both cases, showing a slight negative value (-0.1 to -0.7 bar). Because the

864   location of the fault model changes the boundary between the positive and negative

865   regions, it is difficult to discuss the relationship between ΔCFF and the Zougahana fault

866   based on these results. Nonetheless, the Zougahana fault is not in an area clearly

867   characterized by positive ΔCFF; accordingly, static stress cannot have been an active

868   trigger of the Zougahana fault. In contrast, the Miyaji fault, which has a strike nearly

869   parallel to that of the Zougahana fault, is in a region clearly characterized by positive

870   ΔCFF values of at least 3 bars (Figs. 17b–d). The paleoseismic history suggests that the

871   Futagawa fault may have repeatedly triggered the Zougahana and Miyaji faults,

872   although the triggers may have differed. Figure 17e shows the same analysis results, but

873   when the receiver fault is set to have the sense of movement of the MB I fault. We took

874   the strike of the MB I fault as the value measured on the map, and assumed the fault to

875   be a pure normal fault with a 70°S dip. This assumption is based on the previous

876   interpretation of the fault group northwest of Aso by Fujiwara *et al*. (2016). The results

877   show that the MB I fault clearly belongs to the negative ΔCFF region (<−5.0 bar)

878   regardless of the orientation of the receiver fault. Therefore, static stress cannot be said

879   to be the trigger of MB I fault.

880

881   *The trigger of secondary faulting at the northeast end of the Futagawa fault*

882   The aftershock distribution, strong shaking distribution, and ΔCFF results suggest that

883   the Zougahana fault triggered the strong shaking associated with the main shock (Fig.

884   17a). Nonetheless, it is interesting that a M_j 5.9 earthquake occurred around the

885   Zougahana fault about 1.5 hours after the main shock (JST 03:03) (Fig. 16c). According

886   to the F-net mechanism solution, this earthquake had M_w 5.5, a hypocentral depth of 5

887   km, a N29°E strike, and a slip plane dipping 60° to the northwest. This slip plane sense

888   broadly corresponds to the Zougahana fault. For reference, when using the scaling law

889   for strike-slip faults of Wells and Coppersmith (1994), a M_w 5.5 earthquake can produce

890   a subsurface rupture length of about 2.32 km and a maximum displacement of 0.26 m.

891   The length of the phase discontinuity that appeared along the Zougahana fault was

892   about 4.8 km (Fig. 2), with a horizontal displacement (based on our survey) of 48.6 ±

893   0.2 cm and a vertical displacement of 20.2 ± 4.7 cm (Fig. 6a, b). Such displacement

894 amounts are approximately consistent with the scaling law. In other words, it is

895 impossible to rule out the possibility that the Zougahana fault was activated as a

896 seismogenic with the aftershock about 1.5 hours after the main shock rather than

897 simultaneously with the main shock. Unfortunately, there were no satellite observations

898 between the main shock and this aftershock. Because the area around the Zougahana D

899 prehistoric site is uninhabited, it is difficult to obtain residents' testimonies;

900 accordingly, it remains difficult to determine whether the Zougahana fault was activated

901 at the time of the main shock or the aftershock.

902   In contrast, the trigger of the MB I fault displacement cannot be explained by

903 ΔCFF (Fig. 17e), and there is no aftershock distribution in this area (Fig. 16b–f); it was

904 therefore likely triggered by strong ground shaking at the same time as the main shock.

905 Fujiwara *et al*. (2020) pointed out that the phase discontinuities to the northwest of Aso

906 caldera, including the MB I fault, did not reflect stress changes associated with the main

907 shock, but rather that the displacement was caused by strong ground motions, reflecting

908 the background north–south tensile stress field; we consider their interpretation to be

909 valid. In addition, the results for the Miyaji fault indicate that ΔCFF is a strong

910   candidate as a trigger for displacement there (Figs. 17b–d). Therefore, although the

911   secondary faults around Aso caldera are synchronized to activity on the Futagawa fault,

912   their triggers are diverse. Accordingly, when evaluating secondary faults at the edge of

913   the main fault, assessments based on only one factor will lead to underestimations of the

914   displacement probability of that fault.

915

916   *Role of the Zougahana fault in the tectonics of central Kyushu*

917   The tectonics of the central Kyushu region, including the Futagawa fault, have been the

918   subject of several studies that have produced various models and interpretations.

919   Hatanaka and Shimazaki (1988) interpreted the north–south extensional movement of

920   the BSGZ (Matsumoto, 1979) as a phenomenon in which central and northern Kyushu

921   are displaced dextrally, parallel to the Median Tectonic Line. And they explained that

922   the BSGZ was formed by the Philippine Sea Plate dipping obliquely to the west of the

923   Median Tectonic Line and that the graben group, which runs in an en echelon pattern,

924   formed to relieve the local strain of east–west compression and north–south tension.

925   Chida (1992) divided this graben group into seven individual grabens (including the

926   Beppu Bay, Yufudake, Kuehirayama, Haneyama, and Kudake grabens) and proposed

927   that these grabens formed due to the local east–west compressive stress field within the

928   broader, north–south tensile stress field due to right-lateral movement along the Oita-

929   Kumamoto Tectonic Line, which forms the southern limit of these grabens.

930   Furthermore, Oohashi *et al*. (2020) discussed the tectonic history of central Kyushu by

931   summarizing the strain field of the Futagawa fault and surrounding areas as determined

932   by geological and geodetic methods, as well as the stress field as determined by

933   seismological methods, in the context of existing data. They newly defined the BSGZ as

934   the Central Kyushu Shear Zone (CKSZ), a complex of volcanoes, grabens, and strike-

935   slip faults formed under a transtensional tectonic regime running parallel to the larger

936   structure of the BSGZ. The 2016 Kumamoto earthquake is considered to be a tectonic

937   movement in which dextral slip on the Futagawa-Hinagu Fault Zone (i.e., the southern

938   boundary fault of the CKSZ), the formation of a graben, and the areal subsidence of the

939   Kumamoto Plain to the north boundary of the CKSZ occurred simultaneously.

940   The CKSZ model proposed by Oohashi *et al*. (2020), which incorporates results

941   from the 2016 Kumamoto earthquake and recent geodetic research, is the most

942   reasonable for our interpretation. In this case, the activity of the MB I fault, which is

943   part of the Kuradake graben, can be explained reasonably by transtensional tectonics.

944   However, how should the Zougahana and Miyaji faults be positioned within the model?

945   As revealed by our survey of the Zougahana fault outcrop, the Zougahana fault has

946   repeatedly and similarly slipped since the deposition of the AT tephra ca. 30 ka. In

947   addition, the fault outcrop at Loc. 1 (Figs. 3a, 4b) clearly shows that the fault separates

948   the Aso-2A/2B pyroclastic flow deposit (deposited about 140 ka; Matsumoto *et al*.,

949   1991) (Fig. 5c, d); accordingly, the Zougahana fault may have been active since the

950   Middle Pleistocene. The Aso-4 eruption (ca. 87 ka; Aoki, 2008), which formed the

951   present-day Aso caldera, must have destroyed and buried any active geomorphic

952   structures around Aso caldera, including the Zougahana fault. Still, we may be

953   witnessing a snapshot of the old scar gradually re-emerging due to motions on the

954   Futagawa fault (or other surrounding earthquakes) or the addition of static strain. In

955   other words, the Zougahana and Miyaji faults may not be simple secondary faults in the

956   surface layer, but may be the main shear structures that make up the CKSZ. Figure 18 is

957   a schematic diagram showing the locations and characteristics of the secondary faults

63

958   caused by the 2016 Kumamoto earthquake superimposed on the CKSZ model of

959   Oohashi *et al*. (2020). Although the accuracy of the locations is not sufficient, Oohashi

960   *et al*. (2020) drew inferred dextral faults that pass through Aso caldera, and we suspect

961   that these faults are related to the Zougahana fault and Miyaji fault. In the future, it will

962   be necessary to clarify whether structures corresponding to these secondary faults are

963   hidden beneath the Aso caldera and Mt. Kuju volcanic zones using seismic reflection

964   surveys and detailed aftershock observations. In addition, future studies should consider

965   that secondary faults can form at the contact between active faults and volcanic zones

966   due to various factors.

967

Conclusions

968

969   Following the 2016 Kumamoto earthquake, phase discontinuities were

970   confirmed by InSAR analyses of the Zougahana fault, which is approximately 14 km

971   northeast of the primary Futagawa fault, and a surface rupture was confirmed by a field

972   survey immediately after the 2016 earthquake. In this study, we investigated activity on

973   the Zougahana fault by conducting topographic interpretations, field surveys, and

974   interpretations of fault outcrops, and obtaining multiple cores. As a result, we were able

975   to identify at least six paleoearthquake events, including the 2016 earthquake, on the

976   Zougahana fault. The ages of the four most recent events, which were estimated with

977   relatively high accuracy, were constrained by tephra analyses and the OxCal model

978   using radiocarbon dating, as follows: the AD2016 earthquake and events at 5780–2750

979   cal BP (Event 1), 9020–7200 cal BP (Event 2), and 9430–8450 cal BP (Event 3).

980   Furthermore, it is also thought that multiple events occurred in the period from 29,850

981   to 10,960 cal BP, after deposition of the AT tephra ca. 30 ka, including Events 4 and 5.

982   Despite limited evidence, we hypothesized the occurrence of possible missing events

983   (PM Event 0.5, PM Event 1.5) based on discrepancies among fault offsets. When

984   compared to the paleoseismic history of the Futagawa fault and other secondary faults

985   around Aso caldera that have slipped since the deposition of the K-Ah tephra (ca. 7.3

986   ka), it became clear that the number of events recognized at the Zougahana fault was

987   likely to be an underestimate, supporting our interpretation of possible missing events at

988   the Zougahana fault outcrop.

989   Based on the distribution of aftershocks, seismic intensity, and a Coulomb Stress

990   Change (ΔCFF) analysis of the 2016 Kumamoto earthquake, we interpreted the

991   Zougahana fault's trigger to have been strong seismic shaking associated with the main

992   shock. However, it is currently impossible to determine whether it was triggered at the

993   same time as the main shock or by the M_j 5.9 aftershock that occurred around the

994   Zougahana fault about 1.5 hours later. In contrast, within the same secondary fault, the

995   Matoishi-Bokujo I fault in the northwest of the Aso caldera may have produced normal

996   fault displacement without an aftershock due to strong ground shaking. The Futagawa

997   fault's ΔCFF may have triggered the Miyaji fault inside the caldera. Even if the

998   secondary faults around Aso caldera synchronized to the activity of the Futagawa fault

999   in the past, the specific triggers of their fault motions are diverse. When evaluating

1000   secondary faults at the ends of primary faults, assessments based on only one type of

1001   factor will likely lead to underestimates of the displacement probability of that fault.

1002   Within the transtensional tectonics model (Central Kyushu Shear Zone), which

1003   views the larger structure of the Beppu-Shimabara Graben as a complex of volcanoes,

1004   grabens, and en echelon strike-slip faults, the Zougahana fault may not be a simple

1005   surface secondary fault. Instead, it may belong to the main shear structure. In the future,

1006   it will be necessary to carry out detailed geophysical surveys and aftershock

1007   observations to determine whether structures corresponding to surface secondary faults

1008   are buried underground in the volcanic zone.

1009

1026   fault outcrop PDF (Supplement 1), microphotographs of particles in tephra

1027   samples (Figure S1), major element compositions of glass shards measured

1028   by EPMA (Table S1), and code for the OxCal chronological model of faulting

1029   events (Text S1, S2).

1030

1031   **Declaration of Competing Interests**

1032   The authors declare no competing interests.

1033

1051 **References**

1052 Aoki, K. (2008). Revised age and distribution of ca. 87 ka Aso-4 tephra based

1053   on new evidence from the northwest Pacific Ocean, *Quaternary*

1054   *International* **178**, no. 1, 100–118.

1055 Asano, K., and T. Iwata (2016). Source rupture processes of the foreshock

1056   and mainshock in the 2016 Kumamoto earthquake sequence estimated

1057   from the kinematic waveform inversion of strong motion data, *Earth*

1058   *Planet Sp* **68**, no. 1, 147, doi: 10.1186/s40623-016-0519-9.

1059 Biasi, G. P., and S. G. Wesnousky (2016). Steps and gaps in ground

1060   ruptures: Empirical bounds on rupture propagation, *Bull. Seismol.*

1061   *Soc. Am.* **106**, no. 3, 1110–1124.

1062 Biasi, G. P., and S. G. Wesnousky (2017). Bends and ends of surface

1063   ruptures, *Bull. Seismol. Soc. Am.* **107**, no. 6, 2543–2560.

1064 Boore, D. M. (1972). A Note on the Effect of Simple Topography on Seismic

1065   Sh Waves, *Bull. Seismol. Soc. Am.* **62**, no. 1, 275–284.

1066   Bronk Ramsey, C. (2009). Bayesian Analysis of Radiocarbon Dates,

1067   *Radiocarbon* **51**, no. 01, 337–360, doi: 10.1017/S0033822200033865.

1068   Bronk Ramsey, C. (1995). Radiocarbon Calibration and Analysis of

1069   Stratigraphy: The OxCal Program, *Radiocarbon* **37**, no. 2, 425–430,

1070   doi: 10.1017/s0033822200030903.

1071   Bronk Ramsey, C. (2024). OxCal 4.4, available at

1072   https://c14.arch.ox.ac.uk/oxcal/OxCal.html# (last accessed April 2024).

1073   Chida, N (1992). Active faults in Central Kyushu, Southwest Japan -

1074   Quaternary faulting along thc Median Tectonic Line in Kyushu-, *The*

1075   *memoirs of the Geological Society of Japan* **40**, 39–51 (in Japanese

1076   with English abstract).

1077   Earthquake Research Committee, Headquarters for Earthquake Research

1078   Promotion (2016) Evaluation of the 2016 Kumamoto Earthquake,

1079   available at

1080   http://www.static.jishin.go.jp/resource/monthly/2016/2016_kumamoto.p

1081   df (Last accessed 11 April 2024) (in Japanese)

1082   Fossen, H (2016). Structural Geology, 2nd edition, Cambridge University

1083   Press, 377-400.

1084   Fujiwara, S., T. Nakano, and Y. Morishita (2020). Detection of triggered

1085   shallow slips caused by large earthquakes using L-band SAR

1086   interferometry, *Earth, Planets and Space* **72**, no. 1, 1–23, doi:

1087   10.1186/s40623-020-01239-6.

1088   Fujiwara, S., T. Nishimura, M. Murakami, H. Nakagawa, M. Tobita, and P.

1089   A. Rosen (2000). 2.5-D surface deformation of M6.1 earthquake near

1090   Mt Iwate detected by SAR interferometry, *Geophysical Research*

1091   *Letters* **27**, no. 14, 2049–2052, doi: 10.1029/1999GL011291.

1092   Fujiwara, S., H. Yarai, T. Kobayashi, Y. Morishita, T. Nakano, B. Miyahara,

1093   H. Nakai, Y. Miura, H. Ueshiba, Y. Kakiage, *et al.* (2016). Small-

1094   displacement linear surface ruptures of the 2016 Kumamoto

1095   earthquake sequence detected by ALOS-2 SAR interferometry, *Earth,*

1096   *Planets and Space* **68**, no. 1, 160, doi: 10.1186/s40623-016-0534-x.

1097   Goto, H., H. Tsutsumi, S. Toda, and Y. Kumahara (2017). Geomorphic

1098   features of surface ruptures associated with the 2016 Kumamoto

1099   earthquake in and around the downtown of Kumamoto City, and

1100   implications on triggered slip along active faults, *Earth Planets Space*

1101   **69**, no. 1, 26, doi: 10.1186/s40623-017-0603-9.

1102   Hatanaka, Y., and K. Shimazaki (1988). Rupture process of the 1975 central

1103   Oita, Japan, earthquake, *Journal of Physics of the Earth* **36**, no. 1, 1–

1104   15.

1105   Himematsu, Y., and M. Furuya (2016). Fault source model for the 2016

1106   Kumamoto earthquake sequence based on ALOS-2/PALSAR-2 pixel-

1107   offset data: evidence for dynamic slip partitioning, Earth Planets

1108   Space 68, no. 1, 169, doi: 10.1186/s40623-016-0545-7.

1109   Imaizumi, T., T. Miyauchi, H. Tsutsumi, and T. Nakata (2018). Digital active

1110   fault map of Japan [Revised Edition], University of Tokyo Press,

1111   Tokyo.

1112   Inoue, N., N. Kitada, N. Shibuya, M. Omata, T. Takahama, M. Tonagi, and

1113   K. Irikura (2020). Probabilistic Evaluation of Off-Fault Displacements

1114   of the 2016 Kumamoto Earthquake, *Pure Appl. Geophys.* **177**, no. 5,

1115   2007–2019, doi: 10.1007/s00024-019-02345-7.

1116   International Atomic Energy Agency (2010). Seismic hazards in site

1117   evaluation for nuclear installations. In IAEA Safety Standards Series

1118   No. SSG-9. ViennaResearch : IAEA.

1119   Ishimura, D., S. Toda, T. Ichihara, N. Takahashi, A. Konno, and H. Sato

1120   (2017). A study on surface ruptures around Miyaji, Aso City,

1121   Kumamoto Prefecture, associated with the 2016 Kumamoto

1122   earthquake sequence and upward slip tapering on pit excavation walls,

1123   Act Fault Res, 47, 9–16 (in Japanese with English abstract).

1124   Ishimura, D., H. Tsutsumi, S. Toda, Y. Fukushima, Y. Kumahara, N.

1125   Takahashi, T. Ichihara, and K. Takada (2021). Repeated triggered

1126   ruptures on a distributed secondary fault system: an example from the

1127   2016 Kumamoto earthquake, southwest Japan, *Earth Planets Space*

1128   **73**, no. 1, 39, doi: 10.1186/s40623-021-01371-x.

1129 Ishimura, D., Y. Iwasa, N. Takahashi, R. Tadokoro, and R. Oda (2022).

1130   Paleoseismic events and shallow subsurface structure of the central

1131   part of the Futagawa fault, which generated the 2016 Mw 7.0

1132   Kumamoto earthquake, *Geomorphology* **414**, 108387.

1133 Iwasa, Y., Y. Kumahara, H. Goto, D. Ishimura, and T. Hosoya (2022).

1134   Faulting history of the Futagawa fault zone based on trenching survey

1135   at Komori, Nishihara Village, Kumamoto Prefecture, *Active Fault*

1136   *Research* **2022**, no. 56, 47–58, doi: 10.11462/afr.2022.56_47 (in

1137   Japanese with English abstract).

1138 Kaneda, H., and T. Chiba (2019). Stereopaired morphometric protection

1139   index red relief image maps (Stereo MPI-RRIMs): Effective

1140   visualization of high-resolution digital elevation models for

1141   interpreting and mapping small tectonic geomorphic features, *Bull.*

1142   *Seismol. Soc. Am.* **109**, no. 1, 99–109, doi: 10.1785/0120180166.

1143   Kaneda, H., T. Nakata, H. Tsutsumi, H. Kondo, N. Sugito, Y. Awata, S. S.

1144   Akhtar, A. Majid, W. Khattak, A. A. Awan, R. S. Yeats, H. Ahmad, A.

1145   Muhammad, S. G. Wesnousky, A. B. Kausar (2008). Surface rupture of

1146   the 2005 Kashmir, Pakistan, earthquake and its active tectonic

1147   implications, *Bull. Seismol. Soc. Am.* **98**, no. 2, 521–557, doi:

1148   10.1785/0120070073.

1149   Kim, Y., and D. J. Sanderson (2006). Structural similarity and variety at the

1150   tips in a wide range of strike–slip faults: a review, *Terra Nova* **18**, no.

1151   5, 330–344, doi: 10.1111/j.1365-3121.2006.00697.x.

1152   King, G., and J. Nábělek (1985). Role of Fault Bends in the Initiation and

1153   Termination of Earthquake Rupture, *Science*, **228**, no. 4702, 984–987,

1154   doi: 10.1126/science.228.4702.984.

1155   King, G. C., R. S. Stein, and J. Lin (1994). Static stress changes and the

1156   triggering of earthquakes, *Bull. Seismol. Soc. Am.* **84**, no. 3, 935–953.

1157   Kobayashi, H., K. Koketsu, and H. Miyake (2017). Rupture processes of the

1158   2016 Kumamoto earthquake sequence: Causes for extreme ground

1159   motions, *Geophysical Research Letters* **44**, no. 12, 6002–6010, doi:

1160   10.1002/2017GL073857.

1161   Kobayashi, T., K. Matsuo, R. Ando, T. Nakano, and G. Watanuki, 2025,

1162   High-resolution image on terminus of fault rupture: relationship with

1163   volcanic hydrothermal structure, Geophysical Journal International,

1164   240, no. 2, 1196–1214.

1165   Kubo, H., W. Suzuki, S. Aoi, and H. Sekiguchi (2016). Source rupture

1166   processes of the 2016 Kumamoto, Japan, earthquakes estimated from

1167   strong-motion waveforms, *Earth Planets Space* **68**, no. 1, 161, doi:

1168   10.1186/s40623-016-0536-8.

1169   Kumahara, Y., H. Kaneda, and H. Tsutsumi (Editors) (2022). *Surface*

1170   *Ruptures Associated with the 2016 Kumamoto Earthquake Sequence*

1171   *in Southwest Japan*, Springer Nature Singapore, Singapore, Advances

1172   in Geological Science, doi: 10.1007/978-981-19-1150-7.

1173   Kumahara, Y., M. Torii, T. Nakata, H. Goto, Y. Iwasa, Y. Suzuki, M.

1174   Watanabe, S. Toda, N. Takahashi, M. Okuno (2017). Fault History of

1175   the Northern Part of Futagawa-Hinagu Fault Zone Based on Trench

1176   Survey at Dozon, Mashiki Town and at Kawayo, Minami-Aso Village,

1177   *Programme and Abstracts JSAF 2017 Fall Meeting*, Hiroshima

1178   University, Higashi-Hiroshima, 24–25 November 2017 (in Japanese).

1179 Lettis, W., J. Bachhuber, R. Witter, C. Brankman, C. E. Randolph, A. Barka,

1180   W. D. Page, and A. Kaya (2002). Influence of releasing step-overs on

1181   surface fault rupture and fault segmentation: Examples from the 17

1182   August 1999 Izmit earthquake on the North Anatolian fault, Turkey,

1183   *Bull. Seismol. Soc. Am.* **92**, no. 1, 19–42.

1184 Machida, H., and Arai, F. (2003). *Atlas of Tephra in and around Japan*

1185   *[revised edition]*. University of Tokyo Press, Tokyo (in Japanese).

1186 Matsumoto, A. (1979). Some Problems on Volcanic Activities and Depression

1187   Structures in Kyushu, Japan, *The memoirs of the Geological Society of*

1188   *Japan* **16**, 127-139 (in Japanese with English Abstruct).

1189 Matsumoto, A., K. Uto, K. Ono, and K. Watanabe (1991). K-Ar age

1190   determinations for Aso volcanic rocks : concordance with

1191   volcanostratigraphy and application to pyroclastic flows, *Programme*

1192   *and Abstracts the Volcanological Society of Japan* **1991.2**, 73 (in

1193   Japanese), doi: 10.18940/vsj.1991.2.0_73.

1194   McLean, D. et al., 2020, Constraints on the Timing of Explosive Volcanism

1195   at Aso and Aira Calderas (Japan) Between 50 and 30 ka: New Insights

1196   From the Lake Suigetsu Sedimentary Record (SG14 Core), Geochem

1197   Geophys Geosyst, 21, no. 8, e2019GC008874, doi:

1198   10.1029/2019GC008874.

1199   Miyabuchi, Y., 2009, A 90,000-year tephrostratigraphic framework of Aso

1200   Volcano, Japan, Sedimentary Geology, 220, nos. 3–4, 169–18.

1201   Miyabuchi, Y., H. Hoshizumi, H. Takada, K. Watanabe, and S. Xu (2003).

1202   Pumice-fall deposits from Aso volcano during the past 90,000 years,

1203   southwestern Japan, *Kazan* **48**, no. 2, 195–214 (in Japanese with

1204   English abstract).

1205   Miyabuchi, Y., and S. Sugiyama (2011). 90,000-year phytolith record from

1206   tephra section at the northeastern rim of Aso caldera, Japan,

1207   *Quaternary international* **246**, no. 1–2, 239–246.

1208   Miyakawa, A., T. Sumita, Y. Okubo, R. Okuwaki, M. Otsubo, S. Uesawa, and

1209   Y. Yagi (2016). Volcanic magma reservoir imaged as a low-density body

1210   beneath Aso volcano that terminated the 2016 Kumamoto earthquake

1211   rupture, Earth Planets Space, 68, no. 1, 208, doi: 10.1186/s40623-016-

1212   0582-2.

1213   Miyazawa, M. (2016). An investigation into the remote triggering of the Oita

1214   earthquake by the 2016 Mw 7.0 Kumamoto earthquake using full

1215   wavefield simulation, *Earth Planets Space* **68**, no. 1, 205, doi:

1216   10.1186/s40623-016-0585-z.

1217   Nakata, T., and T. Imaizumi (2002). Digital active fault map of Japan,

1218   University of Tokyo Press, Tokyo (in Japanese).

1219   National Institute of Advanced Industrial Science and Technology (2009)

1220   Active Fault Database of Japan, June 23, 2009 version, available at

1221   https://gbank.gsj.jp/activefault/index_e_gmap.html (Last accessed

1222   March 2025).

1223 National Institute of Advanced Industrial Science and Technology (2025).

1224   Active Fault Database of Japan, February 14, 2025 version, available

1225   at https://gbank.gsj.jp/activefault/index_e_gmap.html (Last accessed

1226   March 2025).

1227 Nishiki, K., J. Itoh, and T. Ueno (2012). Database of Quaternary volcanic

1228   and intrusive rock bodies in Japan, *Geol. Surv. Jpn. Interim Rep* **60** (in

1229   Japanese).

1230 Obata, H. (eds) (1998). The Zougahana D Prehistoric Site in Ichinomiya

1231   Town, Aso Country, Kumamoto Prefecture; Summary Report on First

1232   Excavation, Board of Education, Ichinomiya Town (in Japanese with

1233   English Abstruct).

1234 Okamura, Y., S. Abe, Y. Miyashita, T. Azuma, T. Togo, Y. Shirahama, Y.

1235   Awata, T. Maruyama, T. Ogami, R. Imura, H. Tsutsumi, H. Goto, and

1236   Y. Kumahara (2018). Survey of detailed position and shape of active

1237   faults to understand the fault segments and observation to reveal the

1238   paleoseismic history and slip rates. In: *Research Report of a*

1239   *Comprehensive Active Fault Survey After the 2016 Kumamoto*

1240   *Earthquake*, 2017 Fiscal Year. Ministry of Education, Culture, Sports,

1241   Science and Technology and Kyushu University (in Japanese).

1242   Ono, K. and K. Watanabe (1985). Geological Map of Aso Volcano. *Geological*

1243   *Map of Volcanoes* **4**. Geological Survey of Japan (in Japanese with

1244   English abstract).

1245   Oohashi, K., M. Otsubo, S. Matsumoto, K. Kobayashi, K. Sato, and T.

1246   Nishimura (2020). The Quaternary Tectonics of Central Kyushu and

1247   the 2016 Kumamoto Earthquake: From a Multifaceted Viewpoint

1248   Combining Geology, Seismology, and Geodesy, *Journal of Geography*

1249   *(Chigaku Zasshi)* **129**, no. 4, 565–589, doi: 10.5026/jgeography.129.565

1250   (in Japanese with English abstract).

1251   Ootaki, O., T. Inoue, I. Ueda, T. Yamashita, K. Yamaguchi, H. Shirai, A.

1252   Suzuki, and K. Mikihara (2016). Revision of the Results of Control

1253   Points after the 2016 Kumamoto Earthquake, *Journal of the*

1254   *Geospatial Information Authority of Japan* **128**, 177–187 (in Japanese).

1255   Ozawa, T., E. Fujita, and H. Ueda (2016). Crustal deformation associated

1256   with the 2016 Kumamoto Earthquake and its effect on the magma

1257   system of Aso volcano, *Earth, Planets and Space* **68**, no. 1, 186, doi:

1258   10.1186/s40623-016-0563-5.

1259   Petersen, M. D., T. E. Dawson, R. Chen, T. Cao, C. J. Wills, D. P. Schwartz,

1260   and A. D. Frankel (2011). Fault displacement hazard for strike-slip

1261   faults, *Bull. Seismol. Soc. Am.* **101**, no. 2, 805–825.

1262   Reimer, P. J., W. E. Austin, E. Bard, A. Bayliss, P. G. Blackwell, C. B.

1263   Ramsey, M. Butzin, H. Cheng, R. L. Edwards, and M. Friedrich (2020).

1264   The IntCal20 Northern Hemisphere radiocarbon age calibration curve

1265   (0–55 cal kBP), *Radiocarbon* **62**, no. 4, 725–757.

1266   Saito, K., H. Takahashi, M. Ohzono, and Y. Ohta (2025). Dynamic Stress

1267   Estimation During the M 5.7 Remotely Triggered Earthquake Caused

1268   by the 2016 M 7.0 Kumamoto Earthquake, Kyushu, Japan, Using

1269   Dense Strong-Motion and High-Rate GNSS Data, *Seismological*

1270   *Research Letters*, doi: <u>10.1785/0220240311</u>.

1271   Sato, H. P., K. Komura, H. Une, T. Nakano, and H. Yagi (2021). Study on

1272   Cumulative Activities of Passively Ruptured Faults through a

1273   Trenching Survey at the Matoishi Bokujo I Fault, Northwest Side of

1274   the Aso Caldera, Southwestern Japan, *Geographical review of Japan*

1275   *series A* **94**, no. 4, 250–264, doi: 10.4157/grj.94.250 (in Japanese with

1276   English abstract).

1277   Shirahama, Y., M. Yoshimi, Y. Awata, T. Maruyama, T. Azuma, Y. Miyashita,

1278   H. Mori, K. Imanishi, N. Takeda, T. Ochi, *et al.* (2016). Characteristics

1279   of the surface ruptures associated with the 2016 Kumamoto

1280   earthquake sequence, central Kyushu, Japan, *Earth, Planets and*

1281   *Space* **68**, no. 1, doi: 10.1186/s40623-016-0559-1.

1282   Smith, V. C., R. A. Staff, S. P. E. Blockley, C. Bronk Ramsey, T. Nakagawa,

1283   D. F. Mark, K. Takemura, and T. Danhara (2013). Identification and

1284   correlation of visible tephras in the Lake Suigetsu SG06 sedimentary

1285   archive, Japan: chronostratigraphic markers for synchronising of east

1286   Asian/west Pacific palaeoclimatic records across the last 150 ka,

1287   *Quaternary Science Reviews* **67**, 121–137, doi:

1288   10.1016/J.QUASCIREV.2013.01.026.

1289 Suzuki, Y., D. Ishimura, Y. Kumaki, Y. Kumahara, N. Chida, T. Nakata, and

1290   T. Nakano (2017). 1:25,000 Active Fault Map, Futagawa-Hinagu Fault

1291   Zone and its Vicinity "Aso". Geospatial Information Authority of Japan,

1292   Ibaraki (in Japanese).

1293 Takeuchi, S., K. Toshida, D. Miura, H. Ito, and S. Uesawa, 2021,

1294   Relationships between magmatic properties and eruption magnitude of

1295   explosive eruptions at Japanese arc volcanoes during the last one

1296   hundred thousand years, Journal of Volcanology and Geothermal

1297   Research, 419, 107345.

1298 The Research Group for Active Tectonics in Kyushu (1989). Active Tectonics

1299   in Kyushu. University of Tokyo Press, Bunkyo-ku, Tokyo (in Japanese).

1300   Toda, S. and Ishimura, D. (2019). Evaluation of short active faults reflected

1301   from distributed minor surface breaks found at recent inland large

1302   earthquakes including the 2016 Kumamoto earthquake, *The*

1303   *Quaternary Research (Daiyonki-Kenkyu)* **58**, 2, 121-136 (in Japanese

1304   with English Abstract).

1305   Toda, S., R. S. Stein, V. Sevilgen, and J. Lin (2011). Coulomb 3.3 Graphic-

1306   rich deformation and stress-change software for earthquake, tectonic,

1307   and volcano research and teaching—user guide, 63, available at

1308   https://pubs.usgs.gov/of/2011/1060/ (Last accessed April 2024).

1309   Toda, S., M. Torii, M. Okuno, A. Konno, H. Ono, and N. Takahashi (2019).

1310   Evidence for Holocene paleoseismic events on the 2016 Kumamoto

1311   earthquake rupture zone within the Aso caldera:, *Active Fault*

1312   *Research* **2019**, no. 51, 13–25, doi: 10.11462/afr.2019.51_13 (in

1313   Japanese with English abstract).

1314   Tsutsumi, H., S. Toda, H. Goto, Y. Kumahara, D. Ishimura, N. Takahashi, K.

1315   Taniguchi, M. Omata, Y. Kohriya, M. Gomi, *et al.* (2018). Paleoseismic

1316   trenching across the surface rupture of the 2016 Kumamoto

1317   earthquake at Jichu, Mashiki Town, Kumamoto Prefecture, *Active*

1318   *Fault Research* **2018**, no. 49, 31–39, doi: 10.11462/afr.2018.49_31 (in

1319   Japanese with English abstract).

1320   Uchide, T., H. Horikawa, M. Nakai, R. Matsushita, N. Shigematsu, R. Ando,

1321   and K. Imanishi (2016). The 2016 Kumamoto–Oita earthquake

1322   sequence: aftershock seismicity gap and dynamic triggering in volcanic

1323   areas, *Earth Planets Space* **68**, no. 1, 180, doi: 10.1186/s40623-016-

1324   0556-4.

1325   Ueta, K., R. Miyawaki, K. Iemura, T. Yokoyama, and A. Miyawaki (2018).

1326   Paleoseismological study on surface fault ruptures produced by the

1327   2016 Kumamoto earthquake. In *Japan Geoscience Union Meeting*

1328   *2018*, Makuhari Messe, Chiba, 20–24 May 2018 (in Japanese with

1329   English abstract).

1330   Une, H., T. Nakano, S. Fujiwara, H. P. Sato, and H. Yagi (2022). Surface

1331   Ruptures in the Northwest of the Outer Aso Caldera, in *Surface*

1332   *Ruptures Associated with the 2016 Kumamoto Earthquake Sequence*

1333   *in Southwest Japan* Y. Kumahara, H. Kaneda, and H.

1334   Tsutsumi(Editors), Springer Nature Singapore, Singapore, Advances in

1335   Geological Science, 205–211, doi: 10.1007/978-981-19-1150-7_15.

1336   Watanabe, K., K. Ono, and S. Hiratsuka. (1982). Pumice eruption at

1337   Kusasenrigahama volcano, Bulletin of the Volcanological Society of

1338   Japan, 27, 337–339 (in Japanese).

1339   Watanabe K. (1984). Active Faults in and around Kumamoto, *Journal of the*

1340   *Kumamoto Geoscience Association* **76**, 9–16 (in Japanese) (Translated

1341   by KK).

1342   Watanabe, K., K. Taguchi, H. Obata, S. Okamoto (2001). Examination of

1343   obsidian and its gemstones excavated from the Zougahana D

1344   prehistoric site, Aso, Japan (Preliminary report), *Journal of the*

1345   *Kumamoto Geoscience Association* **127**, 2–9 (in Japanese) (Translated

1346   by KK).

1347 Wells, D. L., and K. J. Coppersmith, 1994, New empirical relationships

1348   among magnitude, rupture length, rupture width, rupture area, and

1349   surface displacement, *Bull. Seismol. Soc. Am.* 84, no. 4, 974–1002.

1350 Wesnousky, S. G. (1988). Seismological and structural evolution of strike-

1351   slip faults, *Nature*, **335**, no. 6188, 340–343, doi: 10.1038/335340a0.

1352 Wesnousky, S. G. (2006). Predicting the endpoints of earthquake ruptures,

1353   *Nature*, **444**, no. 7117, 358–360.

1354 Yarai, H. (2016). Source fault models of the 2016 Kumamoto earthquake

1355   inverted from crustal deformation, *Bulletin of the Geospatial*

1356   *Information Authority of Japan* **128**, 169 (in Japanese).

1357 Yoshida, S. (2016). Earthquakes in Oita triggered by the 2016 M7.3

1358   Kumamoto earthquake, *Earth Planets Space* **68**, no. 1, 176, doi:

1359   10.1186/s40623-016-0552-8.

1360 Yoshida, K., K. Miyakoshi, K. Somei, and K. Irikura (2017). Source process

1361   of the 2016 Kumamoto earthquake (Mj7.3) inferred from kinematic

1362   inversion of strong-motion records, *Earth Planets Space* **69**, no. 1, 64,

1363   doi: 10.1186/s40623-017-0649-8.

1364   Yue, H., Z. E. Ross, C. Liang, S. Michel, H. Fattahi, E. Fielding, A. Moore, Z.

1365   Liu, and B. Jia (2017). The 2016 Kumamoto $M_w = 7.0$ Earthquake: A

1366   Significant Event in a Fault–Volcano System, *JGR Solid Earth* **122**, no.

1367   11, 9166–9183, doi: 10.1002/2017JB014525.

1368   Zhang, Y., X. Shan, G. Zhang, W. Gong, X. Liu, H. Yin, D. Zhao, S. Wen, and

1369   C. Qu (2018). Source model of the 2016 Kumamoto, Japan, earthquake

1370   constrained by InSAR, GPS, and strong-motion data: Fault slip under

1371   extensional stress, *Bull. Seismol. Soc. Am.* **108**, no. 5A, 2675–2686.

1372

1373

1374　**List of Figure Captions**

1375　**Figure 1 (a)** Location of the study area in Kyushu, southwestern Japan. EU,

1376　Eurasia plate; PA, Pacific plate; PH, Philippine Sea plate. **(b)** Topography

1377　and location of the study area in Kyushu. BSGZ, Beppu-Shimabara

1378　Graben Zone; MTL, Median Tectonic Line. **(c)** Location and topographic

1379　map of the epicentral area of the 2016 Kumamoto earthquake. Black

1380　lines indicate traces of active and inferred active faults from Nakata and

1381　Imaizumi (2002), red lines indicate surface rupture traces of the 2016

1382　Kumamoto earthquake from Kumahara *et al.* (2022), and blue lines

1383　represent phase discontinuities identified by Fujiwara *et al.* (2016). The

1384　trace of the Zougahana fault, the main target of this study, is based on

1385　Watanabe (1984). MB I, Matoishi-Bokujo I fault. The background slope

1386　map was created from the Geospatial Information Authority of Japan

1387　(GSI) 10-m-mesh digital elevation model (DEM).

1388

1389   **Figure 2** Interferogram of the Zougahana fault area before and after the

1390   2016 earthquake (location shown in Fig. 1c). The images were taken on 7

1391   March and 18 April 2016 looking south, and created based on GSI maps.

1392

1393   **Figure 3 (a)** Geological map around the Zougahana D prehistoric site based

1394   on Ono and Watanabe (1985) and Obata (1998) (location shown in Fig.

1395   1c). The traces of phase discontinuities and the Zougahana fault are after

1396   Fujiwara *et al.* (2016) and Obata (1998), respectively. **(b)** The model

1397   tephra stratigraphy of the northeastern part of Aso caldera, based on

1398   Miyabuchi and Sugiyama (2011).

1399

1400   **Figure 4 (a)** MPI-RRIM around the Zougahana D prehistoric site based on a

1401   1-m-mesh LiDAR DEM (location shown in Fig. 3a). **(b)** Detailed

1402   geomorphic map of the same area. Background contours at 1 m intervals

1403   were created from the same LiDAR DEM. **(c)** Topographic cross sections

1404   of the scarp along the Zougahana fault (see **(b)** for lines of section).

1405

1406 **Figure 5 (a)** Drone image of the Zougahana fault outcrop viewed from the

1407   west. Intermittent cracks created by the 2016 earthquake apparent in

1408   this view are indicated by red arrows. **(b)** Photograph of the 2016 rupture

1409   that appeared on the paved road in front of the Zougahana fault outcrop.

1410   **(c)** Fault outcrop found about 290 m southwest of the Zougahana fault

1411   outcrop (Loc. 1 shown in Figs. 3a, 4b). **(d)** Geologic interpretation of the

1412   outcrop in **(c)**.

1413

1414 **Figure 6 (a)** Results of horizontal deformation measurements based on the

1415   total station survey along the paved road. The background image is an

1416   aerial photo taken by drone in April 2021 (location shown in Fig. 4b). **(b)**

1417   Measured vertical deformation along the transect shown in **(a)**.

1418

1419 **Figure 7** Pseudo-vertical deformation calculated from the InSAR image of

1420   the same area shown in Figure 3a.

1421

1422 **Figure 8 (a)** Photomosaic and **(b)** sketch interpretation of the Zougahana

1423   fault outcrop. In **(a)** and **(b)**, numbers indicated by the open squares

1424   correspond to the radiocarbon sample numbers in Table 2. Ages in **(b)** are

1425   mean values of the radiocarbon ages (yr BP).

1426

1427 **Figure 9 (a)** Hand coring locations (blue circles). The extent of this map is

1428   the same as in Figure 6a. The background image is an altitude step-color

1429   map created based on drone aerial photography images. **(b)** Geological

1430   columns of the hand auger cores. Sample numbers (in red text) and

1431   correlated tephras are also shown.

1432

1433 **Figure 10** Major element compositions of glass shards from core ZH-2

1434   determined by EPMA analysis.

1435

1436   **Figure 11** Inferred subsurface structure along line A–B (see Fig. 9a) based

1437   on hand cores and the interpretive sketch of the outcrop. The black circles

1438   indicate the survey points based on total station surveying and the

1439   locations of the hand cores.

1440

1441   **Figure 12** Retro-deformation sequence of faulting and sedimentation around

1442   faults F4 to F7 in the interpretive sketch of the wall (see Fig. 8b). See

1443   subsection *Paleoearthquakes and age constraints about Zougahana fault*

1444   *outcrop* in the **Results**.

1445

1446   **Figure 13** Plot of vertical offsets for each fault in each unit.

1447

1448   **Figure 14** **(a)** Age model A of the Zougahana fault outcrop constructed with

1449   OxCal software based on ^{14}C ages, tephras, and constrained ages for each

1450   event. 'R_date' indicates the ^{14}C age of each sample number (Fig. 8b and

1451   Table 2), and 'U' indicates tephra ages. Event ages are rounded to the

1452   nearest decade and presented with a 2σ (95.4%) confidence interval. **(b)**

1453   Age model B includes possible missing events. Here, we have extracted

1454   and shown only events since Event 2.

1455

1456   **Figure 15** Comparison of the paleoseismic histories of **(a)** the primary fault

1457   (Futagawa fault; Ishimura *et al.*, 2022) and its secondary faults: **(b, c)**

1458   models A and B, respectively, for the Zougahana fault (this study), **(d)**

1459   Miyaji fault (Ishimura *et al.*, 2021), and **(e)** Matoishi-Bokujo I fault (Sato

1460   *et al.*, 2021).

1461

1462   **Figure 16 (a)** Background seismicity from Aso caldera to Mt. Yufu in the 10

1463   years preceding the Kumamoto earthquake. **(b–f)** The distribution of

1464   aftershocks in the same area: **(b)** up to 1 hour after the main shock, **(c)** 1–

1465   2 hours after the main shock, **(d)** 2–3 hours after the main shock, **(e)** 3–6

1466   hours after the main shock, and **(f)** 6 hours to 1 month after the main

1467   shock. Cross sections to 20 km depth orthogonal to the Zougahana fault

1468   are shown for all figures. The targeted earthquakes are those shallower

1469   than 20 km depth and stronger than M_j 2. These figures were drawn

1470   using the Visualization System for Subsurface Structures of the National

1471   Institute of Advanced Industrial Science and Technology (AIST). Black

1472   lines in the figure are active fault traces from the National Institute of

1473   Advanced Industrial Science and Technology (2009) and red triangles

1474   indicate the locations of Quaternary volcanoes, from Nishiki *et al.* (2012).

1475

1476 **Figure 17 (a)** Estimated seismic intensity distribution of the main shock of

1477   the 2016 Kumamoto earthquake by the National Research Institute for

1478   Earth Science and Disaster Prevention, based on the J-RISQ (Japan

1479   Real-time Information System for earthQuake) homepage. **(b–e)** Coulomb

1480   stress change (Δ CFF) in the northeastern part of the epicentral area

1481   associated with the slip of the Futagawa fault. The fault model was

1482   adopted from Yarai *et al.* (2016). **(b–d)** Δ CFF resolved **(b)** onto a pure

1483   dextral strike-slip fault, **(c)** onto a dextral and oblique-slip with south-

98

1484   dipping fault, and **(d)** onto a dextral and oblique-slip with north-dipping

1485   fault. In **(b–d)**, the strike of the receiver fault set is the Zogahana fault.

1486   **(e)** Δ CFF resolved onto a normal fault with the same strike and dip as

1487   the MB I fault.

1488

1489   **Figure 18** Schematic illustration showing the characteristics of secondary

1490   faults and illustrating the relationship between the tectonics of central

1491   Kyushu and the tectonics from Aso caldera to Mt. Yufu. The Central

1492   Kyushu Shear Zone and the dextral fault (inferred) are drawn from

1493   Oohashi *et al.* (2020). Black thin lines indicate active faults, and red

1494   triangles indicate the locations of Quaternary volcanoes, whose sources

1495   are the same as in Figure 16.

1496

1497   Figure 1

1498

1499

1500

100

1501   Figure 2

Zougahana F.

0   0.5   1km

Beam dir.
Flight dir.
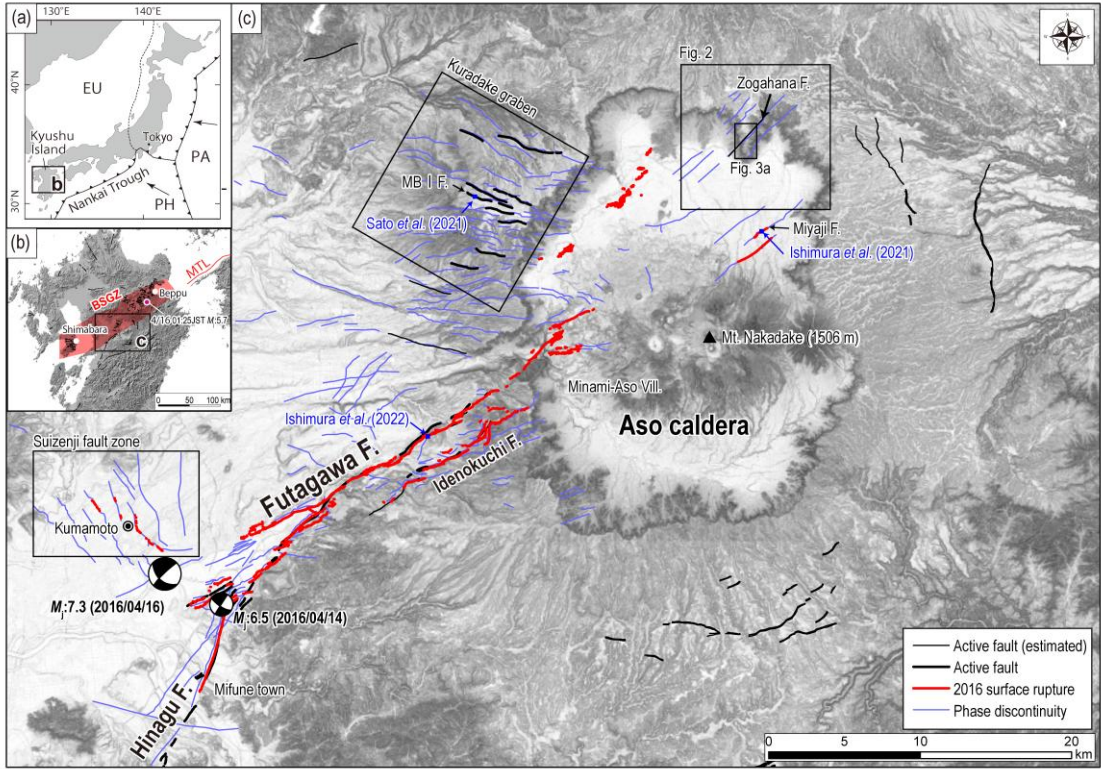
LOS(line of sight, cm)
-12 -9 -6 -3 0 3 6 9 12
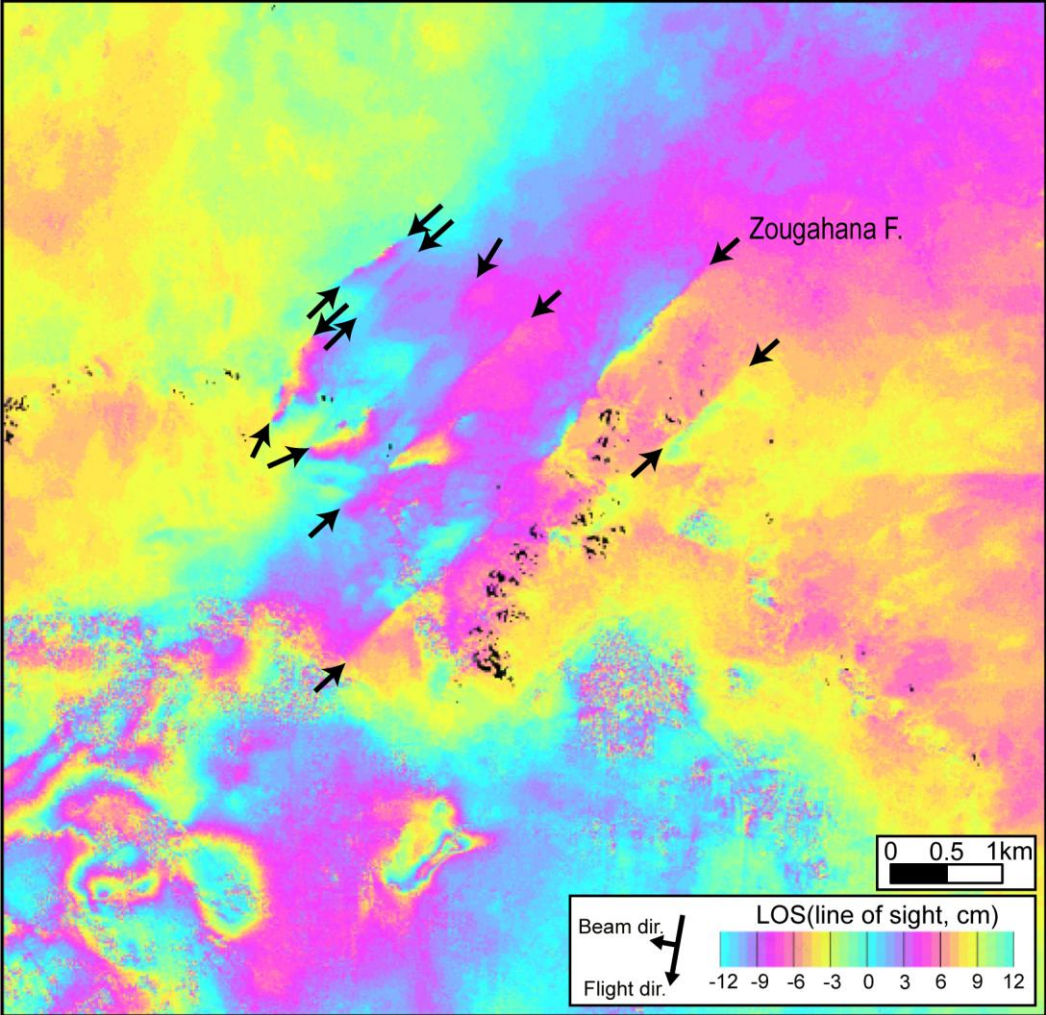
1502

1503

1504

1505

1506

1507
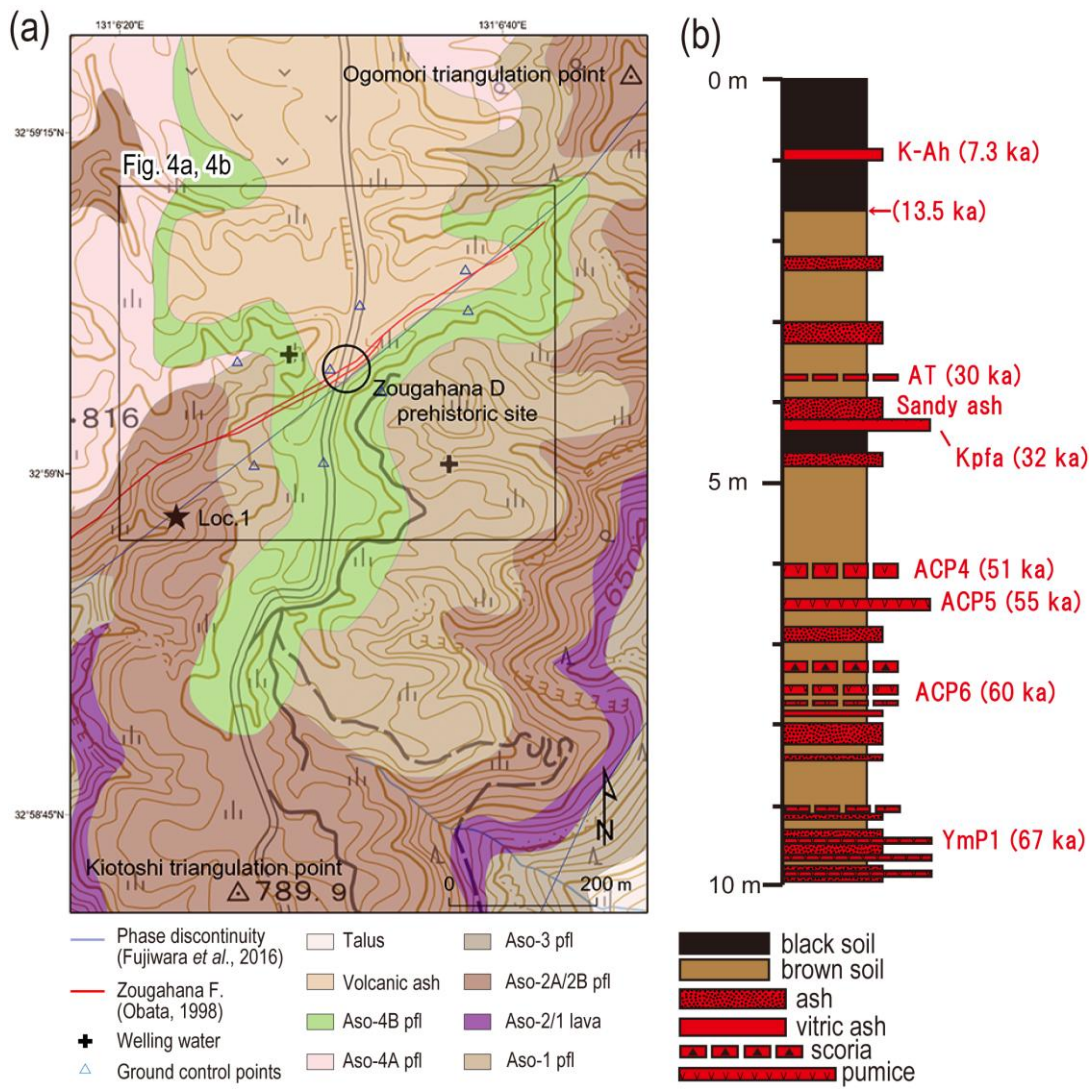
1510   Figure 4
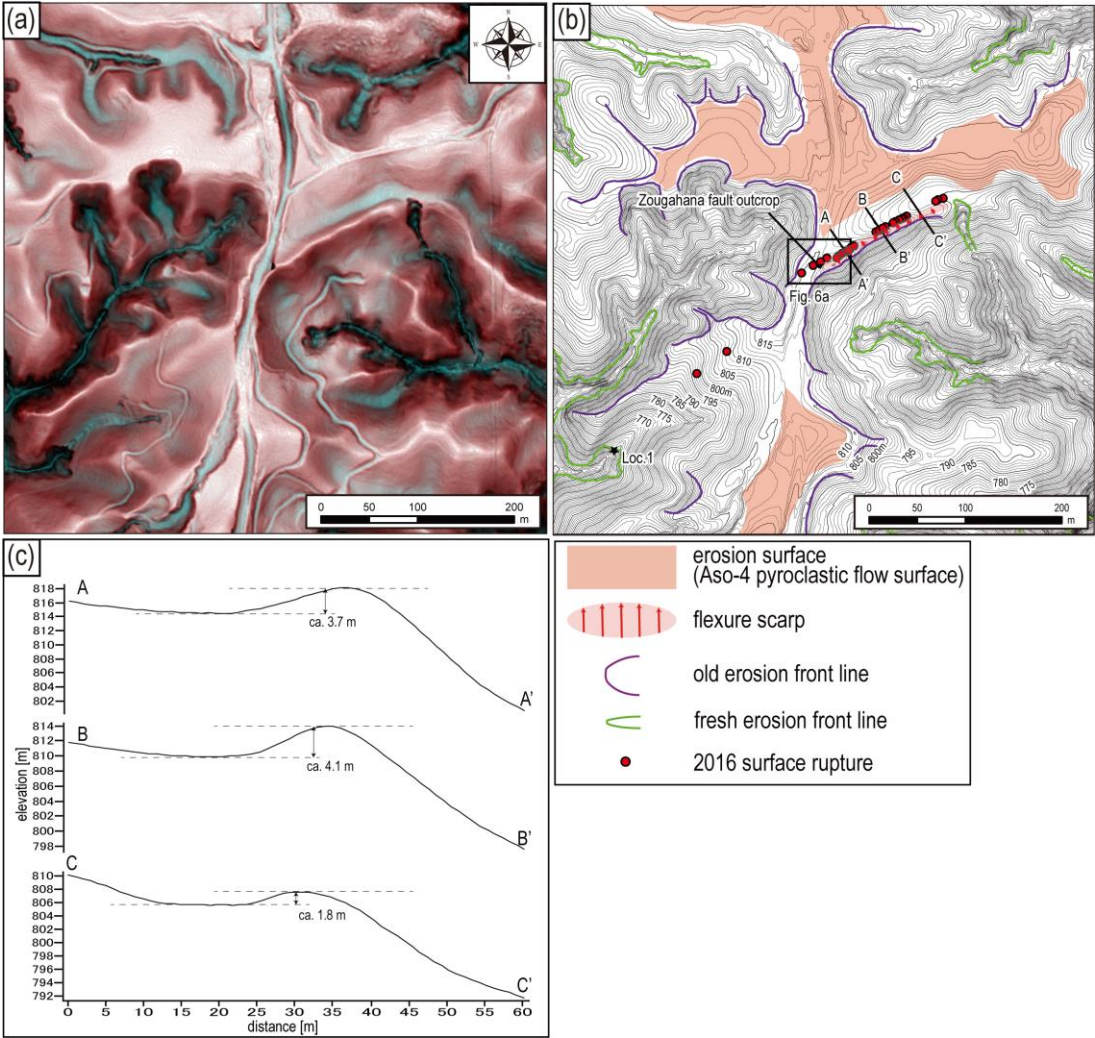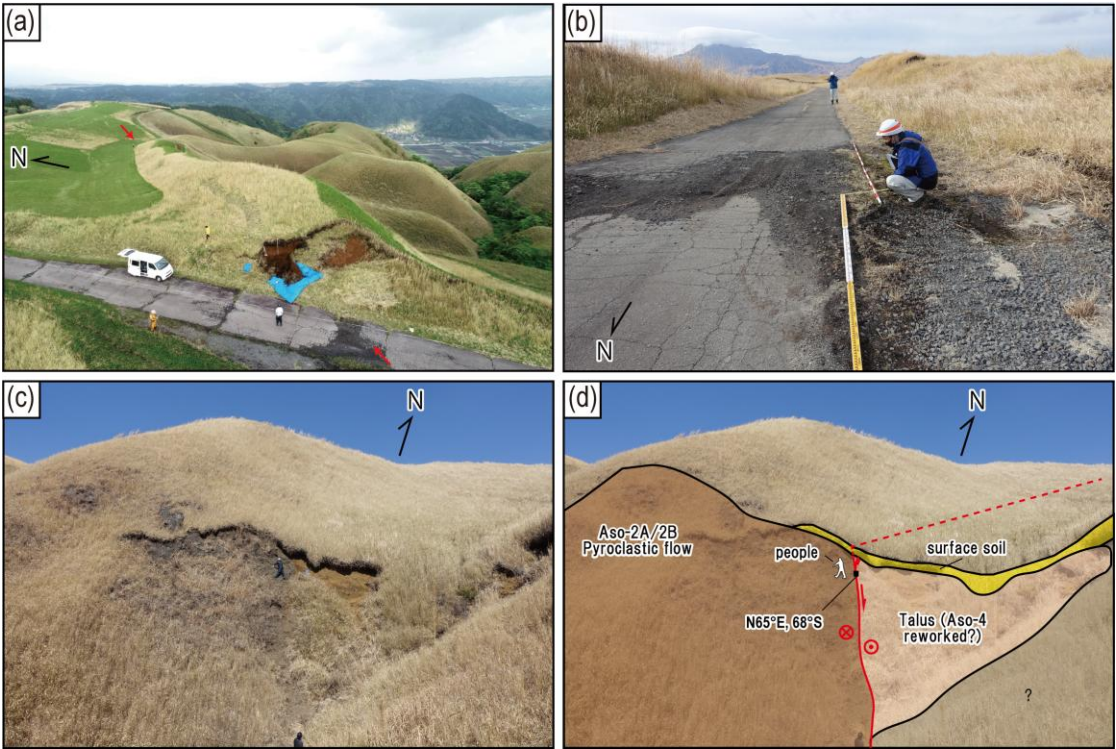

1511

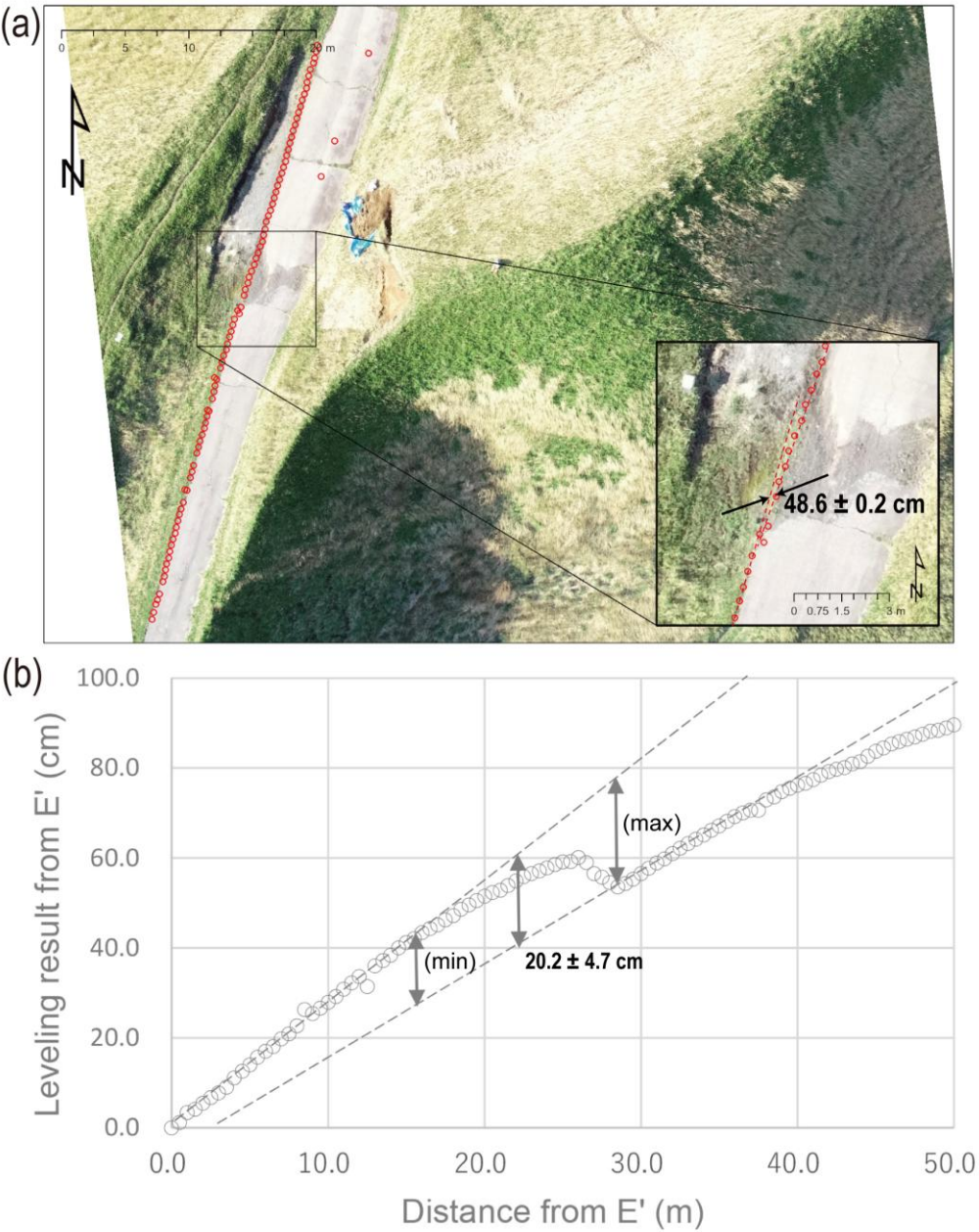1512

1513

1514

1515

1516

1517   Figure 5
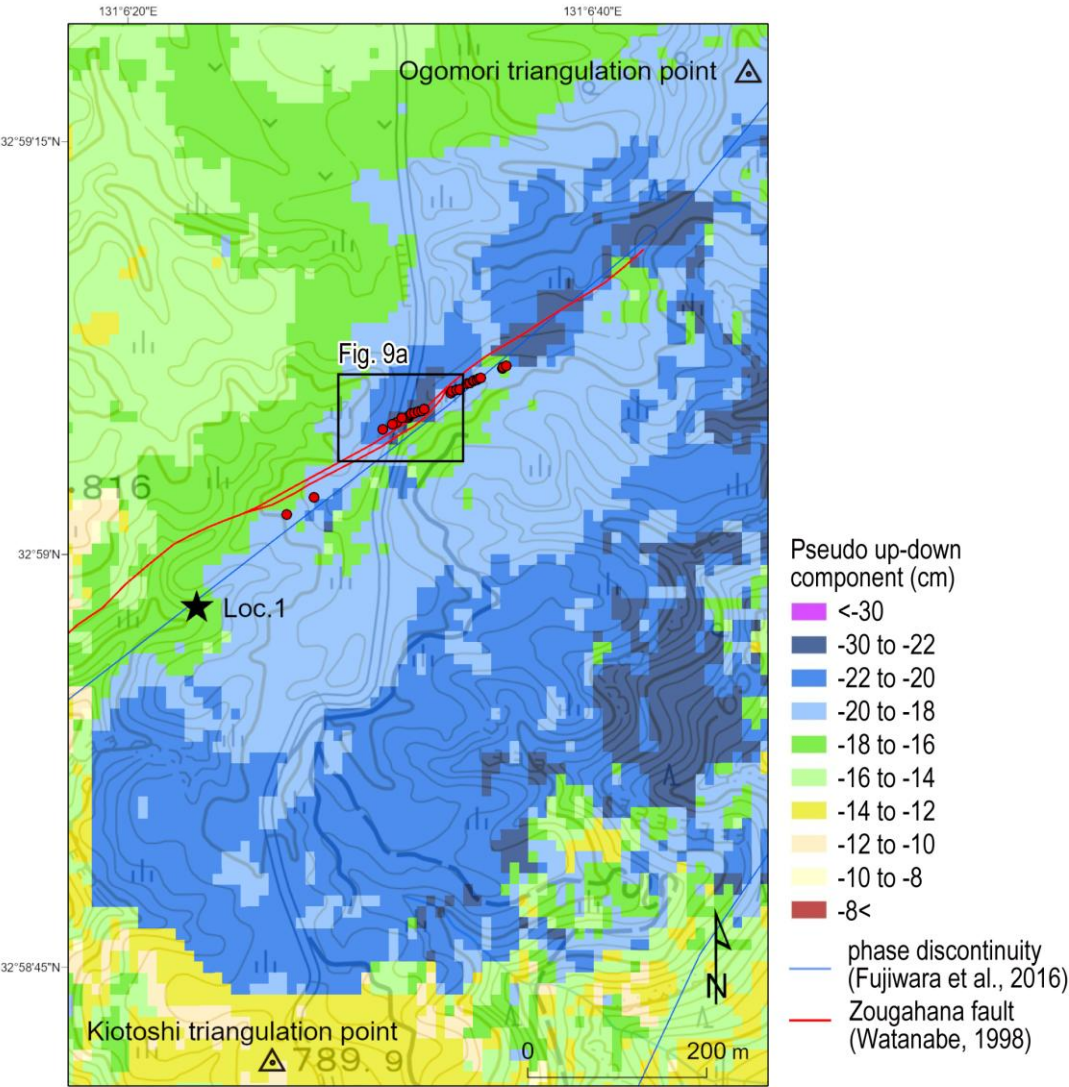

1518

1519

1520

1521

1522

1523

1524   Figure 6

1525

1526

1527

1528   Figure 7

1529

1530
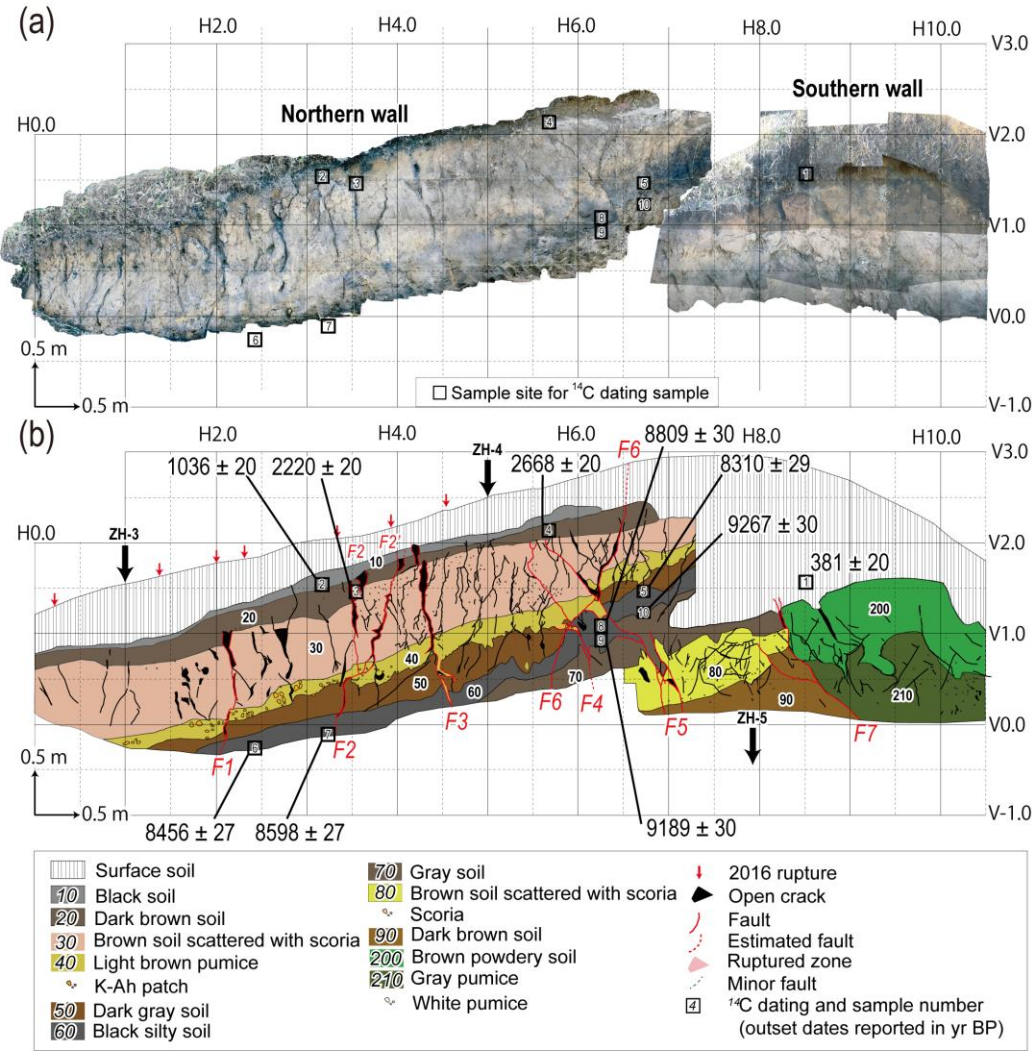
1531

1532

1533

1540   Figure 9
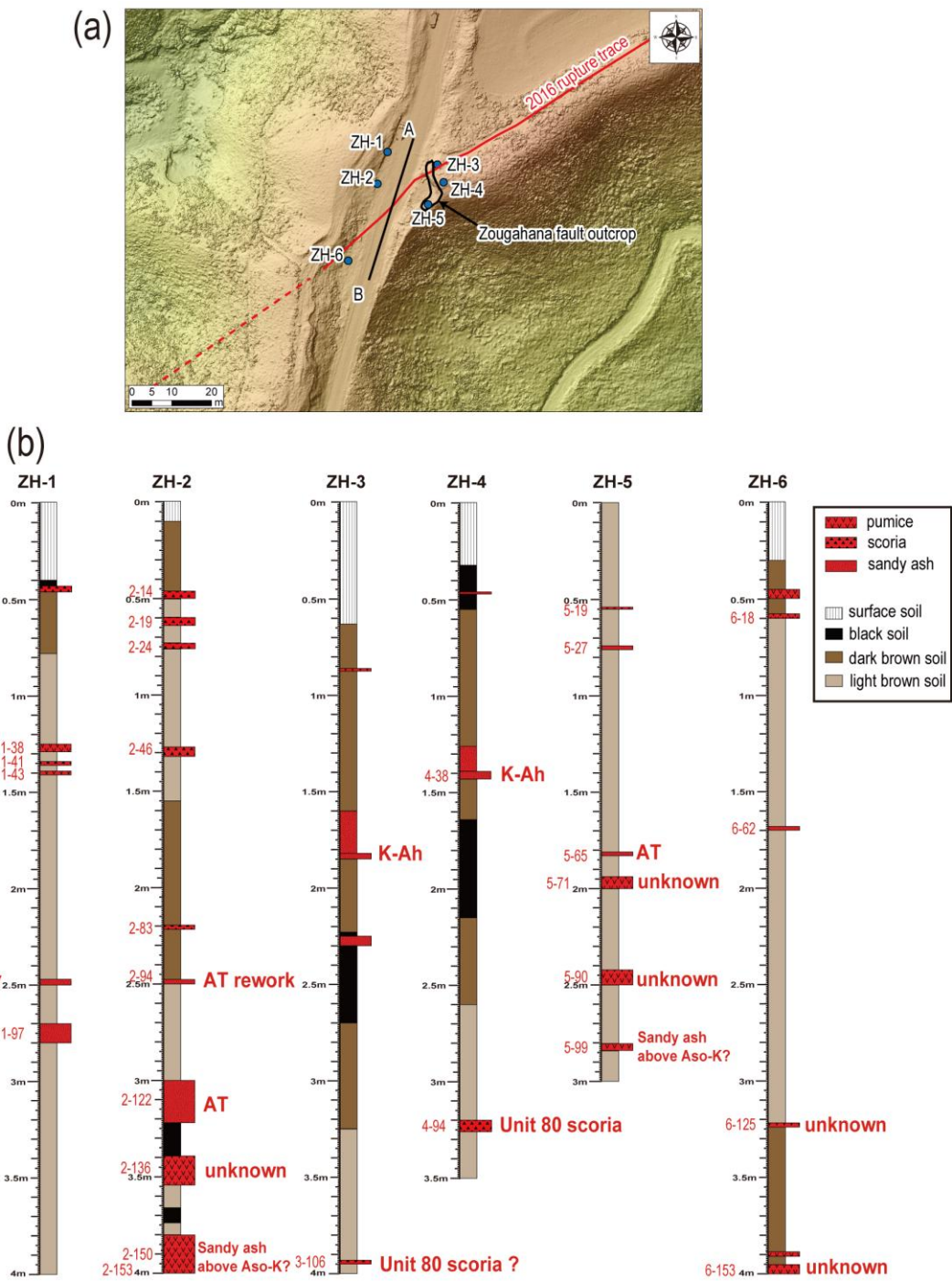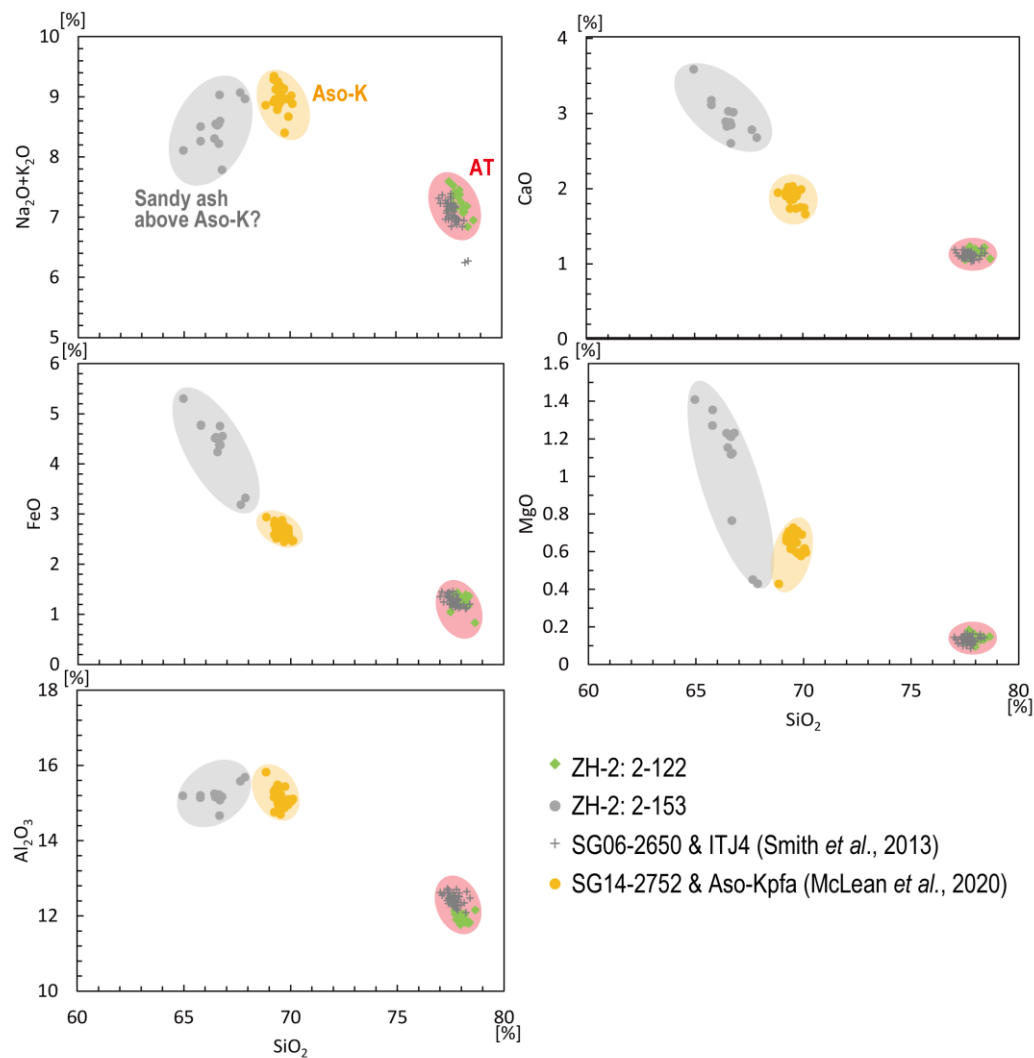
Figure 10

1547   Figure 11

1548

1549

1550

1551

1552

(a) Present
(b) Before 2016 earthquake
(c) Immediately after Event 1
(d) Before Event 1
(e) Immediately after Event 2
(f) Before Event 2
(g) Immediately after Event 3
(h) Before Event 3
(i) Immediately after Event 4
(j) Before Event 4
(k) Immediately after Event 5
(l) Before Event 5
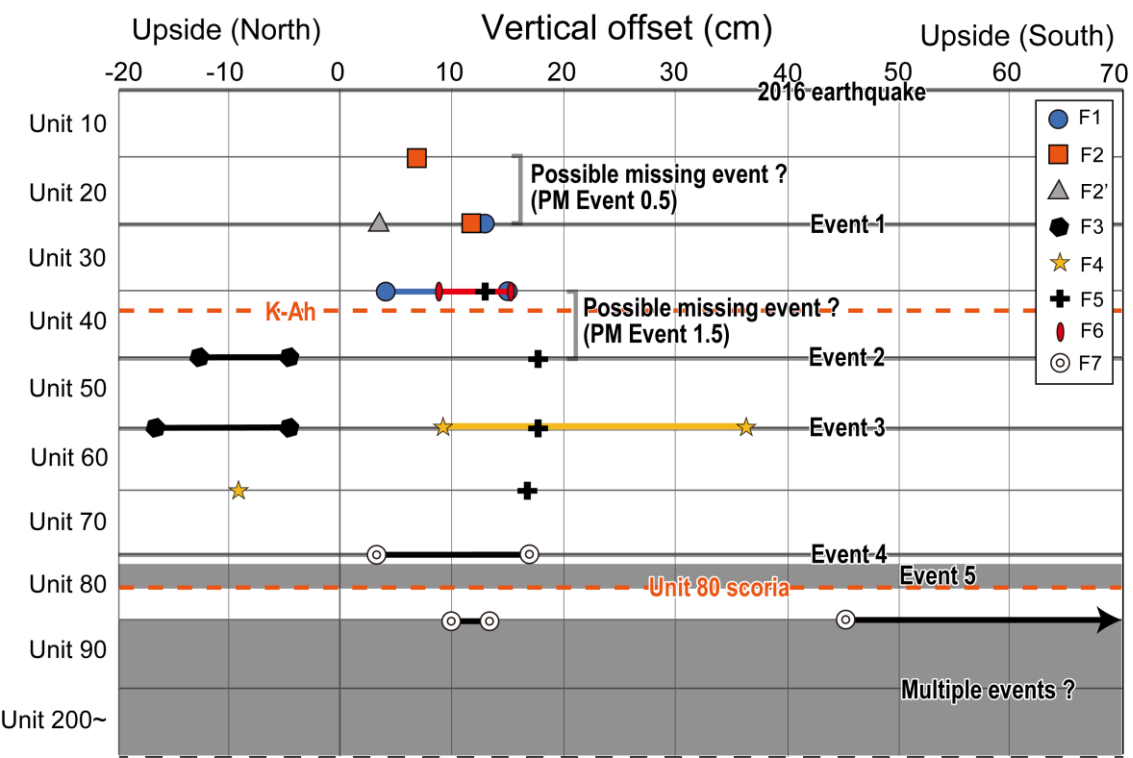
1554
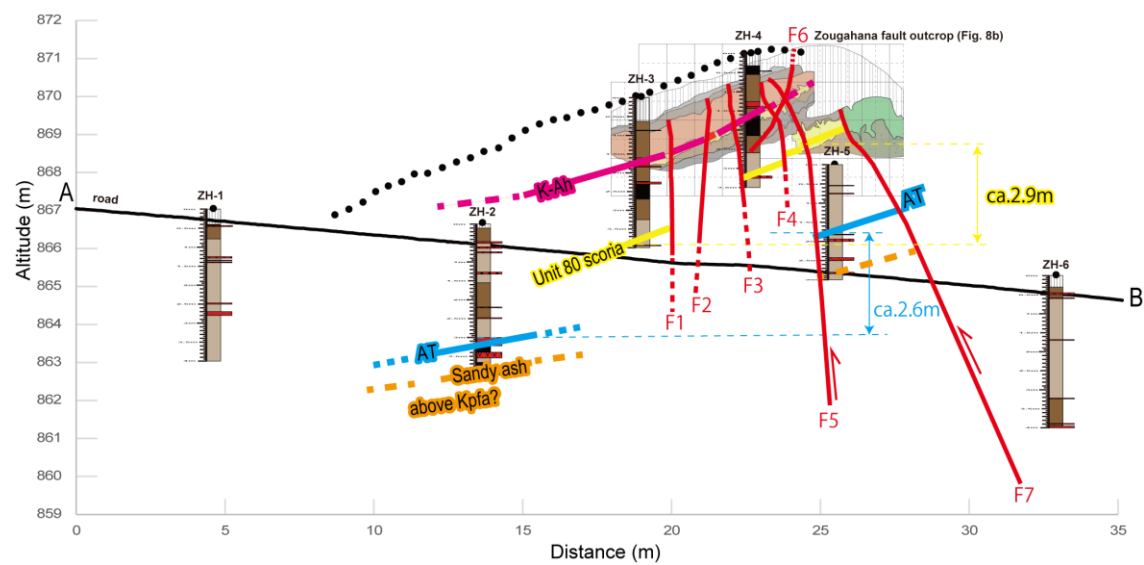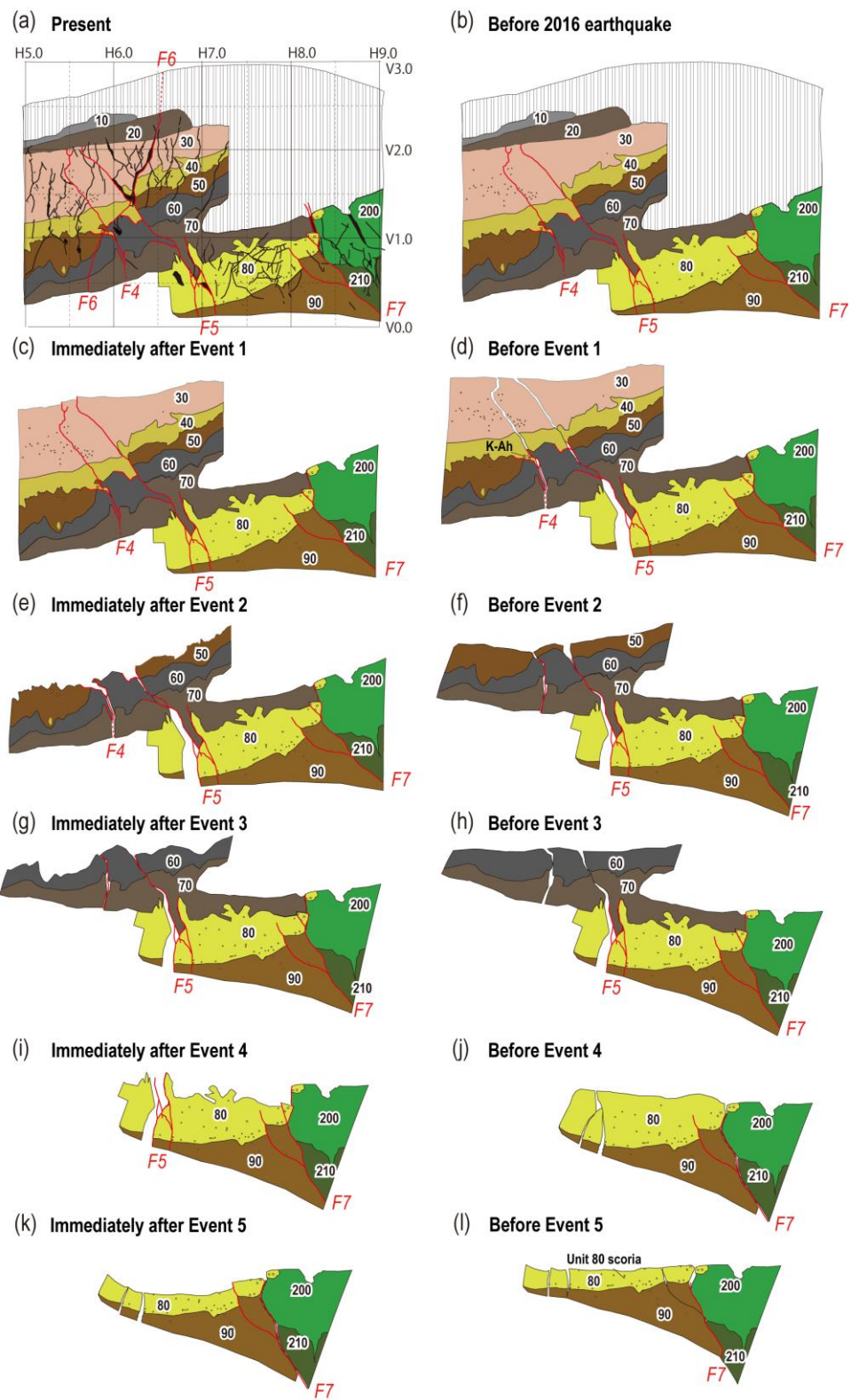
1555   Figure 13

1558   Figure 14
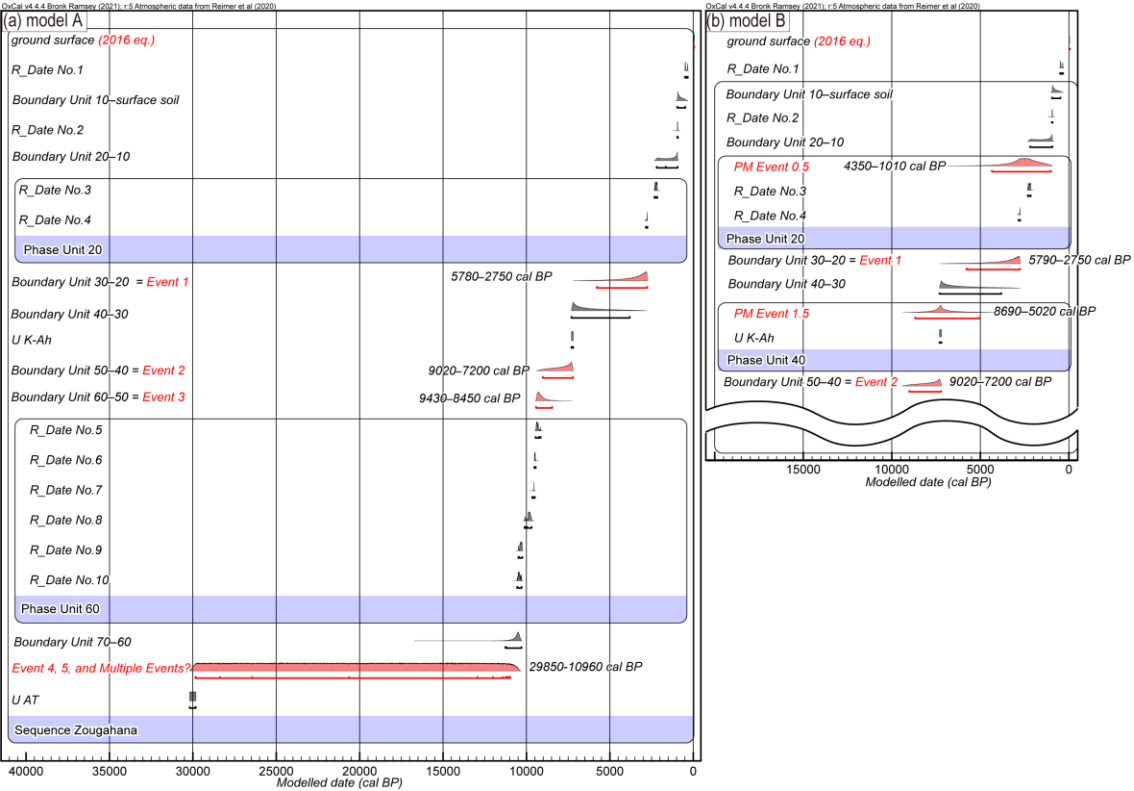
1559

1560

1561

1562

1563

113

1564   Figure 15

(a) Futagawa F. (Ishimura *et al.*, 2022)

Primary fault

K-Ah

2016

2150–1460 cal BP

4310–2940 cal BP

6030–4360 cal BP

(b) Zougahana F. model A (This study)

Event 1

5780–2750 cal BP

Event 2

9020–7200 cal BP

Event 3

9430–8450 cal BP

Event 4, 5, and Multiple Events?

29850–10960 cal BP

2016

(c) Zougahana F. model B (This study)

PM Event 0.5?

4350–1010 cal BP

Event 1

5790–2750 cal BP

PM Event 1.5?

8690–5020 cal BP

Event 2

9020–7200 cal BP

Event 3

9430–8460 cal BP

Event 4, 5, and Multiple Events?

29840–10960 cal BP

2016

Secondary faults

(d) Miyaji F. (Ishimura *et al.*, 2021)

2080–1830 cal BP

2016

(e) Matoishi-Bokujo I F. (Sato *et al.*, 2021)

2810 cal BP–

3430–2890 cal BP

2016

20000   15000   10000   5000   0

Modelled date (cal BP)

1565

1566

114

1567   Figure 16

(a) 2006/04/13~2016/04/13

(b) 2016/04/16/01:25~02:25

(c) 2016/04/16/02:25~03:25

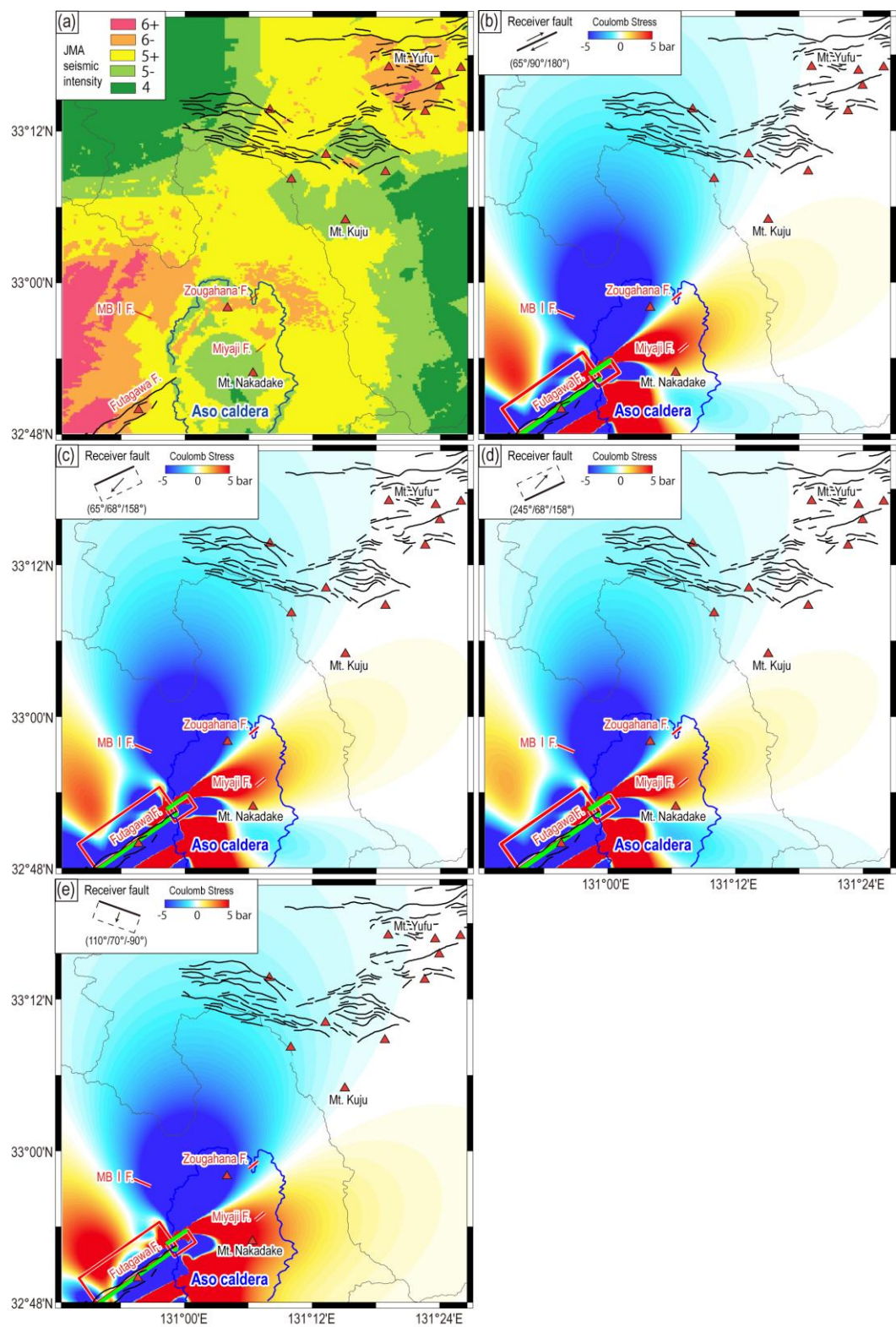(d) 2016/04/16/03:25~04:25

(e) 2016/04/16/04:25~07:25

(f) 2016/04/16/07:25~2016/05/16/07:25

1568

1569

1570

1571

1574   Figure 18

1575

1576

1577